

## RESEARCH ARTICLE

# Coupled thermoelectroelastic analysis of thick and thin laminated piezoelectric structures by exact geometry solid-shell elements based on the sampling surfaces method

Gennady M. Kulikov<sup>1</sup> | Svetlana V. Plotnikova

Laboratory of Intelligent Materials and Structures, Tambov State Technical University, Tambov, Russia

**Correspondence**

Gennady M. Kulikov, Laboratory of Intelligent Materials and Structures, Tambov State Technical University, Sovetskaya Street, 106, Tambov 392000, Russia.

Email: gmkulikov@mail.ru

**Funding information**

Russian Science Foundation, Grant/Award Number: 18-19-00092

**Abstract**

A hybrid-mixed exact geometry four-node thermopiezoelectric solid-shell element through the sampling surfaces (SaS) formulation is proposed. The SaS formulation is based on the choice of an arbitrary number of SaS within layers parallel to the middle surface and located at Chebyshev polynomial nodes in order to introduce the temperatures, displacements and electric potentials of these surfaces as basic shell unknowns. Due to the variational formulation, the outer surfaces and interfaces are also included into a set of SaS. Such choice of unknowns with the use of Lagrange polynomials in the through-thickness approximations of temperatures, temperature gradient, displacements, strains, electric potential, and electric field leads to a very compact higher-order thermopiezoelectric shell formulation. To implement efficient analytical integration throughout the solid-shell element, the extended assumed natural strain method is employed for all components of the temperature gradient, strain tensor, and electric field vector. The developed hybrid-mixed four-node thermopiezoelectric solid-shell element is based on the Hu–Washizu variational principle and shows a superior performance in the case of coarse meshes. It can be useful for the three-dimensional thermoelectroelastic analysis of thick and thin doubly curved laminated piezoelectric shells under thermal loading, since the SaS formulation allows one to obtain the numerical solutions with a prescribed accuracy, which asymptotically approach exact solutions of the theory of thermopiezoelectricity as a number of SaS tends to infinity.

**KEYWORDS**

exact geometry solid-shell element, hybrid-mixed method, sampling surfaces method, thermopiezoelectricity

## 1 | INTRODUCTION

The exact solutions of thermopiezoelectricity are of great importance for the analysis of laminated piezoelectric shells under thermo-electro-mechanical loads due to the fact that the verification of approximate shell theories and shell elements can be assessed by comparing their predictions with exact solutions. The exact analysis of laminated piezoelectric plates and shells under thermal loading has received considerable attention during past 20 years (see review

papers<sup>1,2</sup>). There are at least four approaches to three-dimensional (3D) exact solutions of thermoelectroelasticity for piezoelectric plates, namely, the Pagano approach, the state space approach, the asymptotic expansion approach and the sampling surfaces (SaS) approach. The first approach was implemented for thermopiezoelectric plates in papers.<sup>3-7</sup> The most popular state space approach was effectively used in References 8-12. The 3D solution of thermoelectroelasticity for piezoelectric rectangular plates using the asymptotic expansion approach was obtained by Cheng and Batra.<sup>13</sup> The application of the SaS variational approach to the 3D-coupled thermoelectroelastic analysis of laminated piezoelectric plates was carried out by the authors.<sup>14,15</sup> In the thermopiezoelectric shell formulation, the coefficients of the system of differential equations depend on the thickness coordinate. This means that the Pagano approach and the state space approach cannot be applied to exact solutions for shells. To solve this problem for the thermoelectroelastic cylindrical shells and panels, the power series expansion approach<sup>16-21</sup> and the SaS variational approach<sup>22,23</sup> can be utilized.

Nowadays, the finite element method is a well-established tool for the analysis of smart structures. Since the pioneering work of Allik and Hughes,<sup>24</sup> in which the piezoelectric tetrahedral element was proposed, the finite element analysis of smart structures was carried out in many contributions described in review papers.<sup>25-27</sup>

The static and vibration analysis of composite plates and nanoplates with piezoelectric sensors and actuators using the Kirchhoff plate theory was performed in References 28,29. The thermopiezoelectric shell elements based on the first-order shear deformation theory were developed in papers.<sup>30-33</sup> To describe the temperature and electric potential fields, the layer-wise model is applied.<sup>30,31</sup> The piezoelectric plate elements using the third-order shear deformation theory (TSDT) with the layer-wise description of the electric potential are considered in papers.<sup>34-36</sup> The laminated piezoelectric beam element based on the zigzag TSDT theory with thickness stretching caused by the Poisson effect due to thermal and electric fields is proposed in Reference 37. The finite element formulation in the frame work of the higher-order shear deformation theory (HSDT) for estimating the dynamic response of functionally graded piezoelectric plates was developed in Reference 38. The HSDT layer-wise finite element models for the smart beams and plates under thermo-electro-mechanical loads are considered in papers.<sup>39-43</sup>

Significant progress has been made in developing continuum-based finite elements that can handle the analysis of smart shells satisfactorily.<sup>44-46</sup> These elements are typically defined by two layers of nodes on the outer surfaces of the shell with three displacement degrees of freedom (DOF) and are known as isoparametric six-parameter piezoelectric solid-shell elements. However, the six-parameter solid-shell element formulation based on the complete constitutive equations of thermopiezoelectricity<sup>47,48</sup> is deficient because thickness locking occurs. This is due to the fact that the linear displacement field in the thickness direction results in a constant transverse normal strain, which causes artificial stiffening of the shell element in the case of nonzero Poisson's ratios. To prevent thickness locking, the enhanced assumed strain method can be applied, in which the transverse normal strain is enriched in the thickness direction by a linear term.<sup>44,45</sup>

An effective way of using 3D constitutive equations of thermopiezoelectricity is to employ the higher-order shell theory with seven displacement DOF.<sup>49</sup> The seven-parameter solid-shell element formulation is based on the choice of six displacements of the outer surfaces and the transverse displacement of the middle surface as basic shell unknowns. Such finite element formulation is optimal with respect to the number of DOF. A more general nine-parameter shell theory, in which nine displacements of the bottom, middle, and top surfaces are introduced as shell unknowns was developed later.<sup>50,51</sup> The electric potential is distributed linearly<sup>50</sup> and quadratically<sup>51</sup> through the layers applying a layer-wise description. This piezoelectric solid-shell element formulation is based on the SaS method<sup>22,23</sup> using three equispaced SaS. Such choice of SaS with the use of Lagrange polynomials of the second degree in the through-thickness distributions of displacements, strains and stresses allows the representation of the nine-parameter piezoelectric solid-shell element formulation in a very compact form. Moreover, this higher-order model makes it possible to obtain the Green-Lagrange strain tensor, which exactly represents large rigid-body motions of the shell in any convected curvilinear coordinate system.<sup>52</sup> Taking into account that the displacement vectors of SaS are resolved in the middle surface basis, the nine-parameter shell theory is very promising for the development of exact geometry or geometrically exact (GeX) solid-shell elements.<sup>50,51</sup> The term GeX means that the parametrization of the middle surface is known a priori and, therefore, the coefficients of the first and second fundamental forms and Christoffel symbols are taken exactly at the element nodes.

It is well known that seven- and nine-parameter solid-shell elements cannot be used to evaluate transverse components of the stress tensor and the electric displacement vector in laminated piezoelectric shell structures. For their correct assessment, taking into account the boundary conditions on the outer surfaces and the continuity conditions on the interfaces, one should utilize solid-shell elements based on the higher-order layer-wise theory or solid elements. The solid

elements for piezoelectric beams and plates under thermal loading are discussed in References 53–58. Some authors<sup>56,57</sup> use brick elements from the ABAQUS and ANSYS software packages for static and dynamic thermoelectroelastic analysis of piezoelectric plates. However, the results on the through-thickness distributions of the transverse components of the stress tensor and the electric displacement vector are not documented in these papers. To the authors' knowledge, there are also no results in the literature concerning the prediction of these components in piezoelectric shells under thermal loading using higher-order layer-wise models owing to the inability of these models to take into account thickness stretching.

This paper is intended to solve this problem by developing GeX solid-shell elements based on the SaS layer-wise theory<sup>22,23</sup> to accurately calculate stresses and electric displacements in *thick* and *thin* laminated thermopiezoelectric shell structures. This is one of the main motivations for the present research. Due to the SaS concept, we introduce in the  $n$ th layer  $I_n$  SaS parallel to the middle surface in order to introduce temperatures  $T^{(n)i_n}$ , displacements  $u_i^{(n)i_n}$  and electric potentials  $\varphi^{(n)i_n}$  of these surfaces as fundamental shell unknowns, where  $i_n = 1, 2, \dots, I_n; n = 1, 2, \dots, N; N$  is the number of layers. Such choice of unknowns with the use of Lagrange polynomials of degree  $I_n - 1$  in the through-the-thickness approximations of temperature, temperature gradient and heat flux vector, displacements, strains and stresses, electric potential, electric field and electric displacement vector, as well as the entropy density of the  $n$ th layer leads to a reliable higher-order layer-wise shell formulation, in which *all basic variables* are related to SaS. Recently, the SaS formulation was utilized to develop GeX four-node solid-shell elements for the geometrically linear and nonlinear analysis of piezoelectric shell structures.<sup>59–61</sup> Here, these studies are extended to analyze coupled thermo-electro-mechanical fields in laminated piezoelectric shells.

To prevent shear and membrane locking in the GeX SaS-based four-node solid-shell element, the assumed interpolations of stresses and displacement-independent strains are employed. Therefore, it is necessary to apply the Hu-Washizu mixed variational principle of thermopiezoelectricity.<sup>49</sup> The developed finite element formulation has some computational advantages compared with isoparametric hybrid-mixed piezoelectric solid-shell element formulations.<sup>44–47</sup> This is due to the fact that all elemental matrices are evaluated without costly numerical matrix inversion. It is impossible within the framework of the isoparametric hybrid-mixed shell element formulation.<sup>62,63</sup> The important feature of the GeX thermopiezoelectric solid-shell element is the use of effective analytical integration throughout the finite element using the extended assumed natural strain (ANS) method.<sup>51,59,60</sup>

## 2 | HIGHER-ORDER HEAT TRANSFER THEORY OF LAMINATED SHELLS

Consider a laminated shell of the thickness  $h$ . Let the middle surface  $\Omega$  be described by orthogonal curvilinear coordinates  $\theta_1$  and  $\theta_2$ , which are referred to the lines of principal curvatures of its surface. The coordinate  $\theta_3$  is oriented along the unit vector  $\mathbf{e}_3(\theta_1, \theta_2)$  normal to the middle surface. Introduce the following notations:  $\mathbf{e}_\alpha(\theta_1, \theta_2)$  are the orthonormal base vectors of the middle surface;  $A_\alpha(\theta_1, \theta_2)$  are the coefficients of the first fundamental form;  $k_\alpha(\theta_1, \theta_2)$  are the principal curvatures of the middle surface;  $c_\alpha = 1 + k_\alpha \theta_3$  are the components of the shifter tensor;  $c_\alpha^{(n)i_n}(\theta_1, \theta_2)$  are the components of the shifter tensor on SaS of the  $n$ th layer  $\Omega^{(n)i_n}$  given by

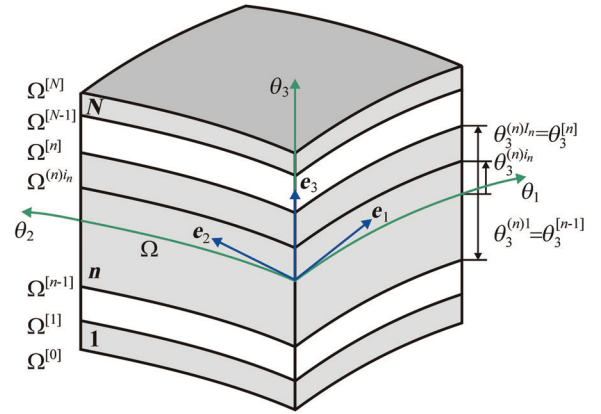
$$c_\alpha^{(n)i_n} = 1 + k_\alpha \theta_3^{(n)i_n}, \quad (1)$$

where  $\theta_3^{(n)i_n}$  are the distances from the middle surface to the SaS of the  $n$ th layer defined as

$$\theta_3^{(n)1} = \theta_3^{[n-1]}, \quad \theta_3^{(n)I_n} = \theta_3^{[n]}, \quad (2)$$

$$\theta_3^{(n)m_n} = \frac{1}{2} (\theta_3^{[n-1]} + \theta_3^{[n]}) - \frac{1}{2} h_n \cos \left( \pi \frac{2m_n - 3}{2(I_n - 2)} \right), \quad (3)$$

where  $h_n = \theta_3^{[n]} - \theta_3^{[n-1]}$  is the thickness of the  $n$ th layer;  $\theta_3^{[m]}$  are the distances from the middle surface to the interfaces  $\Omega^{[m]}$  (Figure 1); the index  $n$  identifies the belonging of any quantity to the  $n$ th layer and runs from 1 to  $N$ ; the index  $m$  identifies the belonging of any quantity to the interface and runs from 1 to  $N - 1$ ; the indices  $i_n, j_n, k_n$  running from 1 to  $I_n$  describe the SaS of the  $n$ th layer, whereas the indices  $m_n$  running from 2 to  $I_n - 1$  describe the inner SaS of the  $n$ th layer;  $N$  is the number of layers;  $I_n$  is the number of SaS of the  $n$ th layer;  $N_{\text{SaS}} = \sum_n I_n - N + 1$  is the total number of SaS; Latin indices  $i, j, k, l$  range from 1 to 3; Greek indices  $\alpha, \beta$  range from 1 to 2.

**FIGURE 1** Geometry of the laminated shell

It is seen from Equation (3) that the inner SaS  $\Omega^{(n)m_n}$  are located at Chebyshev polynomial nodes (roots of the Chebyshev polynomial of degree  $I_n - 2$ ). This fact has a great meaning for the convergence of the SaS method.<sup>14,22</sup>

In an orthonormal basis  $\mathbf{e}_i$ , the relationship between the temperature  $T^{(n)}$  and the temperature gradient  $\Gamma_i^{(n)}$  of the  $n$ th layer is given by

$$\Gamma_\alpha^{(n)} = \frac{1}{A_\alpha c_\alpha} T_{,\alpha}^{(n)}, \quad \Gamma_3^{(n)} = T_{,3}^{(n)}, \quad \theta_3^{[n-1]} \leq \theta_3 \leq \theta_3^{[n]}, \quad (4)$$

where the symbol  $(\dots)_i$  stands for the partial derivatives with respect to coordinates  $\theta_i$ .

As constitutive equations, we consider the Fourier heat conduction equations

$$q_i^{(n)} = -\kappa_{ij}^{(n)} \Gamma_j^{(n)}, \quad \theta_3^{[n-1]} \leq \theta_3 \leq \theta_3^{[n]}, \quad (5)$$

where  $q_i^{(n)}$  are the components of the heat flux vector of the  $n$ th layer;  $\kappa_{ij}^{(n)}$  are the components of the thermal conductivity tensor of the  $n$ th layer. Here and in the following developments, the summation on repeated Latin indices is implied.

Now we introduce the first assumption of the SaS thermopiezoelectric shell formulation. Assume that the temperature, temperature gradient and heat flux are distributed through the thickness of the  $n$ th layer as follows:

$$\left[ T^{(n)} \Gamma_i^{(n)} q_i^{(n)} \right] = \sum_{i_n} L^{(n)i_n} \left[ T^{(n)i_n} \Gamma_i^{(n)i_n} q_i^{(n)i_n} \right], \quad \theta_3^{[n-1]} \leq \theta_3 \leq \theta_3^{[n]}, \quad (6)$$

where  $T^{(n)i_n}(\theta_1, \theta_2)$  are the temperatures of SaS of the  $n$ th layer;  $\Gamma_i^{(n)i_n}(\theta_1, \theta_2)$  and  $q_i^{(n)i_n}(\theta_1, \theta_2)$  are the components of the temperature gradient and heat flux vector of SaS of the  $n$ th layer;  $L^{(n)i_n}(\theta_3)$  are the Lagrange polynomials of degree  $I_n - 1$  defined as

$$L^{(n)i_n} = \prod_{j_n \neq i_n} \frac{\theta_3 - \theta_3^{(n)j_n}}{\theta_3^{(n)i_n} - \theta_3^{(n)j_n}}. \quad (7)$$

The use of Equations (4)–(7) leads to heat conduction equations in terms of SaS variables

$$\Gamma_\alpha^{(n)i_n} = \frac{1}{A_\alpha c_\alpha^{(n)i_n}} T_{,\alpha}^{(n)i_n}, \quad \Gamma_3^{(n)i_n} = \sum_{j_n} M^{(n)j_n} \left( \theta_3^{(n)i_n} \right) T^{(n)j_n}, \quad (8)$$

$$q_i^{(n)i_n} = -\kappa_{ij}^{(n)} \Gamma_j^{(n)i_n}, \quad (9)$$

where  $M^{(n)j_n} = L_{,3}^{(n)j_n}$  are the polynomials of degree  $I_n - 2$ ; their values on SaS are calculated as

$$\begin{aligned}
M^{(n)j_n} \left( \theta_3^{(n)i_n} \right) &= \frac{1}{\theta_3^{(n)j_n} - \theta_3^{(n)i_n}} \prod_{k_n \neq i_n, j_n} \frac{\theta_3^{(n)i_n} - \theta_3^{(n)k_n}}{\theta_3^{(n)j_n} - \theta_3^{(n)k_n}} \text{ for } j_n \neq i_n, \\
M^{(n)i_n} \left( \theta_3^{(n)i_n} \right) &= - \sum_{j_n \neq i_n} M^{(n)j_n} \left( \theta_3^{(n)i_n} \right).
\end{aligned} \tag{10}$$

It is seen from Equation (8) that the transverse component of the temperature gradient  $\Gamma_3^{(n)i_n}$  is represented as a linear combination of temperatures of SaS of the  $n$ th layer  $T^{(n)j_n}$ .<sup>64</sup>

### 3 | SOLID-SHELL ELEMENT FOR HEAT CONDUCTION ANALYSIS OF SHELLS

The variational equation of the heat conduction theory for the laminated shell can be expressed as

$$\delta J = 0, \tag{11}$$

where  $J$  is the basic functional of the heat conduction theory<sup>22</sup> given by

$$\begin{aligned}
J &= \iint_{\Omega} \sum_n \int_{\theta_3^{[n-1]}}^{\theta_3^{[n]}} \frac{1}{2} q_i^{(n)} \Gamma_i^{(n)} A_1 A_2 c_1 c_2 d\theta_1 d\theta_2 d\theta_3 \\
&\quad - \iint_{\Omega^+} \left[ \hat{q}_3^+ T^{[N]} + \frac{1}{2} h^+ \left( T^{[N]} - \hat{T}_c^+ \right)^2 \right] A_1 A_2 c_1^+ c_2^+ d\theta_1 d\theta_2 \\
&\quad + \iint_{\Omega^-} \left[ \hat{q}_3^- T^{[0]} - \frac{1}{2} h^- \left( T^{[0]} - \hat{T}_c^- \right)^2 \right] A_1 A_2 c_1^- c_2^- d\theta_1 d\theta_2 - \iint_{\Sigma} \hat{q}_n T_{\Sigma} d\Sigma,
\end{aligned} \tag{12}$$

where  $T^{[0]}$  and  $T^{[N]}$  are the temperatures of the bottom and top surfaces  $\Omega^- = \Omega^{[0]}$  and  $\Omega^+ = \Omega^{[N]}$  (Figure 1);  $\hat{T}_c^-$  and  $\hat{T}_c^+$  are the prescribed temperatures for the convective transfer on the outer surfaces;  $\hat{q}_3^-$  and  $\hat{q}_3^+$  are the prescribed heat fluxes on the outer surfaces;  $T_{\Sigma}$  and  $\hat{q}_n$  are the temperature and prescribed heat flux at the edge surface  $\Sigma$ ;  $h^-$  and  $h^+$  are the convective heat transfer coefficients;  $c_{\alpha}^- = 1 - k_{\alpha} h/2$  and  $c_{\alpha}^+ = 1 + k_{\alpha} h/2$  are the components of the shifter tensor of outer surfaces. Each outer surface is divided into three parts on which the temperature, heat flux and convective heat transfer are prescribed.

Substituting through-the-thickness distributions of the temperature gradient and heat flux (6) in Equation (12) and considering the first-type boundary conditions on the edge surface, and introducing weighted coefficients<sup>64</sup>

$$\Lambda^{(n)i_n j_n} = \int_{\theta_3^{[n-1]}}^{\theta_3^{[n]}} L^{(n)i_n} L^{(n)j_n} c_1 c_2 d\theta_3, \tag{13}$$

we obtain the variational equation of the heat conduction theory in terms of the SaS variables

$$\begin{aligned}
&\delta \iint_{\Omega} \sum_n \sum_{i_n} \sum_{j_n} \frac{1}{2} \Lambda^{(n)i_n j_n} \left( \Gamma^{(n)i_n} \right)^T \mathbf{k}^{(n)} \Gamma^{(n)j_n} A_1 A_2 d\theta_1 d\theta_2 \\
&= - \iint_{\Omega^+} \left[ \hat{q}_3^+ + h^+ \left( T^{[N]} - \hat{T}_c^+ \right) \right] \delta T^{[N]} A_1 A_2 c_1^+ c_2^+ d\theta_1 d\theta_2 \\
&\quad + \iint_{\Omega^-} \left[ \hat{q}_3^- - h^- \left( T^{[0]} - \hat{T}_c^- \right) \right] \delta T^{[0]} A_1 A_2 c_1^- c_2^- d\theta_1 d\theta_2,
\end{aligned} \tag{14}$$

where

$$\begin{aligned} \Gamma^{(n)i_n} &= \left[ \Gamma_1^{(n)i_n} \Gamma_2^{(n)i_n} \Gamma_3^{(n)i_n} \right]^T, \\ \mathbf{\kappa}^{(n)} &= \begin{bmatrix} \kappa_{11}^{(n)} & \kappa_{12}^{(n)} & 0 \\ \kappa_{21}^{(n)} & \kappa_{22}^{(n)} & 0 \\ 0 & 0 & \kappa_{33}^{(n)} \end{bmatrix}. \end{aligned} \tag{15}$$

The finite element formulation is based on simple interpolation of temperatures of SaS of the  $n$ th layer by a GeX four-node solid-shell element<sup>52,60</sup>

$$T^{(n)i_n} = \sum_r N_r T_r^{(n)i_n}, \tag{16}$$

$$N_r = \frac{1}{4} (1 + n_{1r}\xi_1) (1 + n_{2r}\xi_2), \tag{17}$$

$$n_{1r} = \begin{cases} 1 & \text{for } r = 1, 4 \\ -1 & \text{for } r = 2, 3 \end{cases}, \quad n_{2r} = \begin{cases} 1 & \text{for } r = 1, 2 \\ -1 & \text{for } r = 3, 4 \end{cases},$$

where  $N_r(\xi_1, \xi_2)$  are the bilinear shape functions of the element;  $T_r^{(n)i_n}$  are the temperatures of SaS of the  $n$ th layer at the element nodes;  $\xi_1$  and  $\xi_2$  are the normalized curvilinear coordinates  $\theta_1$  and  $\theta_2$  (Figure 2); the nodal index  $r$  runs from 1 to 4.

To implement analytical integration throughout the element, the extended ANS method<sup>52,60</sup> can be applied to interpolate temperature gradients of SaS of the  $n$ th layer

$$\Gamma^{(n)i_n} = \sum_r N_r \Gamma_r^{(n)i_n}, \tag{18}$$

$$\Gamma_r^{(n)i_n} = \left[ \Gamma_{1r}^{(n)i_n} \Gamma_{2r}^{(n)i_n} \Gamma_{3r}^{(n)i_n} \right]^T,$$

where  $\Gamma_r^{(n)i_n}$  are the temperature gradients of SaS of the  $n$ th layer at element nodes, which are evaluated as

$$\Gamma_r^{(n)i_n} = \mathbf{B}_{\theta_r}^{(n)i_n} \mathbf{T}, \tag{19}$$

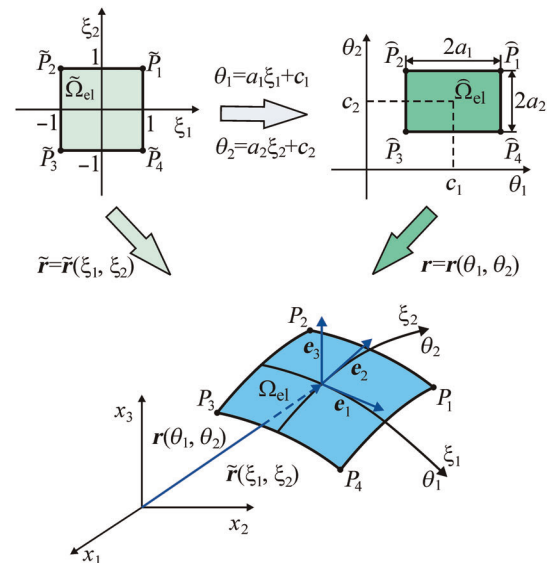


**FIGURE 2** Biunit square in  $(\xi_1, \xi_2)$ -space mapped into the middle surface of the geometrically exact four-node solid-shell element in  $(x_1, x_2, x_3)$ -space

where  $\mathbf{B}_{\theta_r}^{(n)i_n}$  are the *constant* matrices of order  $3 \times 4N_{\text{SaS}}$  presented in Appendix A;  $\mathbf{T}$  is the temperature vector of the solid-shell element given by

$$\mathbf{T} = [\mathbf{T}_1^T \mathbf{T}_2^T \mathbf{T}_3^T \mathbf{T}_4^T]^T, \quad (20)$$

$$\mathbf{T}_r = [T_r^{[0]} T_r^{(1)2} \dots T_r^{(1)I_1-1} T_r^{[1]} T_r^{(2)2} \dots T_r^{(N-1)I_{N-1}-1} T_r^{[N-1]} T_r^{(N)2} \dots T_r^{(N)I_N-1} T_r^{[N]}]^T,$$

where  $T_r^{[0]}$  and  $T_r^{[N]}$  are the temperatures of the outer surfaces at element nodes;  $T_r^{[m]}$  and  $T_r^{(n)m_n}$  are the temperatures of interfaces and inner SaS of the  $n$ th layer at element nodes.

To represent the GeX thermal solid-shell element formulation in a compact form, we write the ANS interpolation (18) as follows:

$$\begin{aligned} \mathbf{\Gamma}^{(n)i_n} &= \sum_{r_1, r_2} (\xi^1)^{r_1} (\xi^2)^{r_2} \mathbf{\Gamma}_{r_1 r_2}^{(n)i_n}, \\ \mathbf{\Gamma}_{r_1 r_2}^{(n)i_n} &= \left[ \mathbf{\Gamma}_{1r_1 r_2}^{(n)i_n} \mathbf{\Gamma}_{2r_1 r_2}^{(n)i_n} \mathbf{\Gamma}_{3r_1 r_2}^{(n)i_n} \right]^T. \end{aligned} \quad (21)$$

Here and below, the indices  $r_1$  and  $r_2$  run from 0 to 1. Using Equations (18)–(21), we obtain

$$\mathbf{\Gamma}_{r_1 r_2}^{(n)i_n} = \mathbf{B}_{\theta r_1 r_2}^{(n)i_n} \mathbf{T}, \quad (22)$$

where  $\mathbf{B}_{\theta r_1 r_2}^{(n)i_n}$  are the constant matrices of order  $3 \times 4N_{\text{SaS}}$  given by

$$\mathbf{B}_{\theta r_1 r_2}^{(n)i_n} = \frac{1}{4} \left[ \mathbf{B}_{\theta 1}^{(n)i_n} + (1 - 2r_1) \mathbf{B}_{\theta 2}^{(n)i_n} + (1 - 2r_1)(1 - 2r_2) \mathbf{B}_{\theta 3}^{(n)i_n} + (1 - 2r_2) \mathbf{B}_{\theta 4}^{(n)i_n} \right]. \quad (23)$$

Substituting interpolations (16) and (21) into the variational equation (14) and replacing the geometric parameters of the middle surface  $A_\alpha$  and  $k_\alpha$  with their values at the element center, we can analytically integrate throughout the finite element. As a result, the following system of algebraic equations is obtained:

$$(\mathbf{K}_{\theta\theta}^b + \mathbf{K}_{\theta\theta}^c) \mathbf{T} = \mathbf{F}_\theta, \quad (24)$$

where  $\mathbf{K}_{\theta\theta}^b$  is the basic thermal stiffness matrix defined as

$$\mathbf{K}_{\theta\theta}^b = \sum_{r_1+r_2 \leq 2} \frac{1}{3^{r_1+r_2}} \sum_n \sum_{i_n} \sum_{j_n} \Lambda^{(n)i_n j_n} \left( \mathbf{B}_{\theta r_1 r_2}^{(n)i_n} \right)^T \mathbf{k}^{(n)} \mathbf{B}_{\theta r_1 r_2}^{(n)j_n}, \quad (25)$$

$\mathbf{K}_{\theta\theta}^c$  is the stiffness matrix corresponding to the convective heat transfer and  $\mathbf{F}_\theta$  is the thermal surface vector presented in Appendix A.

## 4 | HIGHER-ORDER THERMOELECTROELASTIC THEORY OF LAMINATED SHELLS

Here, we introduce the second assumption of the SaS thermopiezoelectric shell formulation. Assume that the displacements  $u_i^{(n)}$ , strains  $\varepsilon_{ij}^{(n)}$ , stresses  $\sigma_{ij}^{(n)}$ , electric potential  $\varphi^{(n)}$ , electric field  $E_i^{(n)}$ , electric displacements  $D_i^{(n)}$ , and entropy density  $S^{(n)}$  are distributed through the thickness of the  $n$ th layer<sup>14,22</sup> as follows:

$$\begin{aligned} & \left[ u_i^{(n)} \varepsilon_{ij}^{(n)} \sigma_{ij}^{(n)} \varphi^{(n)} E_i^{(n)} D_i^{(n)} S^{(n)} \right] \\ &= \sum_{i_n} \mathcal{L}^{(n)i_n} \left[ u_i^{(n)i_n} \varepsilon_{ij}^{(n)i_n} \sigma_{ij}^{(n)i_n} \varphi^{(n)i_n} E_i^{(n)i_n} D_i^{(n)i_n} S^{(n)i_n} \right], \quad \theta_3^{[n-1]} \leq \theta_3 \leq \theta_3^{[n]}, \end{aligned} \quad (26)$$

where  $u_i^{(n)i_n}(\theta_1, \theta_2)$ ,  $\varepsilon_{ij}^{(n)i_n}(\theta_1, \theta_2)$ ,  $\sigma_{ij}^{(n)i_n}(\theta_1, \theta_2)$ ,  $\varphi^{(n)i_n}(\theta_1, \theta_2)$ ,  $E_i^{(n)i_n}(\theta_1, \theta_2)$ ,  $D_i^{(n)i_n}(\theta_1, \theta_2)$ , and  $S^{(n)i_n}(\theta_1, \theta_2)$  are the displacements, strains, stresses, electric potential, electric field, electric displacements, and entropy density of SaS of the  $n$ th layer, respectively.

In the orthonormal basis  $\mathbf{e}_i$ , the relations between strains and displacements of SaS of the  $n$ th layer<sup>52</sup> can be written as

$$\begin{aligned} 2\varepsilon_{\alpha\beta}^{(n)i_n} &= \frac{1}{c_\beta^{(n)i_n}} \lambda_{\alpha\beta}^{(n)i_n} + \frac{1}{c_\alpha^{(n)i_n}} \lambda_{\beta\alpha}^{(n)i_n}, \\ 2\varepsilon_{\alpha 3}^{(n)i_n} &= \frac{1}{c_\alpha^{(n)i_n}} \lambda_{3\alpha}^{(n)i_n} + \beta_\alpha^{(n)i_n}, \quad \varepsilon_{33}^{(n)i_n} = \beta_3^{(n)i_n}, \end{aligned} \tag{27}$$

where  $\lambda_{i\alpha}^{(n)i_n}(\theta_1, \theta_2)$  and  $\beta_i^{(n)i_n}(\theta_1, \theta_2)$  are the strain parameters of SaS of the  $n$ th layer defined as

$$\begin{aligned} \lambda_{\alpha\alpha}^{(n)i_n} &= \frac{1}{A_\alpha} u_{\alpha,\alpha}^{(n)i_n} + B_\alpha u_\beta^{(n)i_n} + k_\alpha u_3^{(n)i_n} \text{ for } \beta \neq \alpha, \\ \lambda_{\beta\alpha}^{(n)i_n} &= \frac{1}{A_\alpha} u_{\beta,\alpha}^{(n)i_n} - B_\alpha u_\alpha^{(n)i_n} \text{ for } \beta \neq \alpha, \\ \lambda_{3\alpha}^{(n)i_n} &= \frac{1}{A_\alpha} u_{3,\alpha}^{(n)i_n} - k_\alpha u_\alpha^{(n)i_n}, \quad B_\alpha = \frac{1}{A_\alpha A_\beta} \text{ for } \beta \neq \alpha, \end{aligned} \tag{28}$$

$$\beta_i^{(n)i_n} = \sum_{J_n} M^{(n)j_n}(\theta_3^{(n)i_n}) u_i^{(n)j_n}. \tag{29}$$

In the orthonormal basis  $\mathbf{e}_i$ , the relations between the electric field and electric potentials of SaS of the  $n$ th layer<sup>60</sup> are expressed as

$$\begin{aligned} E_\alpha^{(n)i_n} &= -\frac{1}{A_\alpha c_\alpha^{(n)i_n}} \varphi_{,\alpha}^{(n)i_n}, \\ E_3^{(n)i_n} &= -\sum_{J_n} M^{(n)j_n}(\theta_3^{(n)i_n}) \varphi^{(n)j_n}. \end{aligned} \tag{30}$$

For simplicity, we consider the case of linear piezoelectric materials. Therefore, the constitutive equations of thermopiezoelectricity in terms of SaS variables<sup>22</sup> are

$$\boldsymbol{\sigma}^{(n)i_n} = \mathbf{C}^{(n)} \boldsymbol{\varepsilon}^{(n)i_n} - (\mathbf{e}^{(n)})^T \mathbf{E}^{(n)i_n} - \boldsymbol{\gamma}^{(n)} \Theta^{(n)i_n}, \tag{31}$$

$$\mathbf{D}^{(n)i_n} = \mathbf{e}^{(n)} \boldsymbol{\varepsilon}^{(n)i_n} + \boldsymbol{\epsilon}^{(n)} \mathbf{E}^{(n)i_n} + \mathbf{r}^{(n)} \Theta^{(n)i_n}, \tag{32}$$

$$S^{(n)i_n} = (\boldsymbol{\gamma}^{(n)})^T \boldsymbol{\varepsilon}^{(n)i_n} + (\mathbf{r}^{(n)})^T \mathbf{E}^{(n)i_n} + \chi^{(n)} \Theta^{(n)i_n}, \tag{33}$$

where

$$\begin{aligned} \boldsymbol{\varepsilon}^{(n)i_n} &= \left[ \varepsilon_{11}^{(n)i_n} \quad \varepsilon_{22}^{(n)i_n} \quad \varepsilon_{33}^{(n)i_n} \quad 2\varepsilon_{12}^{(n)i_n} \quad 2\varepsilon_{13}^{(n)i_n} \quad 2\varepsilon_{23}^{(n)i_n} \right]^T, \\ \boldsymbol{\sigma}^{(n)i_n} &= \left[ \sigma_{11}^{(n)i_n} \quad \sigma_{22}^{(n)i_n} \quad \sigma_{33}^{(n)i_n} \quad \sigma_{12}^{(n)i_n} \quad \sigma_{13}^{(n)i_n} \quad \sigma_{23}^{(n)i_n} \right]^T, \\ \mathbf{E}^{(n)i_n} &= \left[ E_1^{(n)i_n} \quad E_2^{(n)i_n} \quad E_3^{(n)i_n} \right]^T, \quad \mathbf{D}^{(n)i_n} = \left[ D_1^{(n)i_n} \quad D_2^{(n)i_n} \quad D_3^{(n)i_n} \right]^T, \\ \mathbf{C}^{(n)} &= \begin{bmatrix} C_{1111}^{(n)} & C_{1122}^{(n)} & C_{1133}^{(n)} & C_{1112}^{(n)} & 0 & 0 \\ C_{2211}^{(n)} & C_{2222}^{(n)} & C_{2233}^{(n)} & C_{2212}^{(n)} & 0 & 0 \\ C_{3311}^{(n)} & C_{3322}^{(n)} & C_{3333}^{(n)} & C_{3312}^{(n)} & 0 & 0 \\ C_{1211}^{(n)} & C_{1222}^{(n)} & C_{1233}^{(n)} & C_{1212}^{(n)} & 0 & 0 \\ 0 & 0 & 0 & 0 & C_{1313}^{(n)} & C_{1323}^{(n)} \\ 0 & 0 & 0 & 0 & C_{2313}^{(n)} & C_{2323}^{(n)} \end{bmatrix}, \end{aligned} \tag{34}$$



$$\mathbf{e}^{(n)} = \begin{bmatrix} 0 & 0 & 0 & 0 & e_{113}^{(n)} & e_{123}^{(n)} \\ 0 & 0 & 0 & 0 & e_{213}^{(n)} & e_{223}^{(n)} \\ e_{311}^{(n)} & e_{322}^{(n)} & e_{333}^{(n)} & e_{312}^{(n)} & 0 & 0 \end{bmatrix},$$

$$\mathbf{\epsilon}^{(n)} = \begin{bmatrix} \epsilon_{11}^{(n)} & \epsilon_{12}^{(n)} & 0 \\ \epsilon_{21}^{(n)} & \epsilon_{22}^{(n)} & 0 \\ 0 & 0 & \epsilon_{33}^{(n)} \end{bmatrix},$$

$$\boldsymbol{\gamma}^{(n)} = [\gamma_{11}^{(n)} \gamma_{22}^{(n)} \gamma_{33}^{(n)} \gamma_{12}^{(n)} 0 0]^T, \quad \mathbf{r}^{(n)} = [0 0 r_3^{(n)}]^T,$$

where  $\Theta^{(n)i_n} = T^{(n)i_n} - T_0$  is the temperature rise of the SaS of the  $n$ th layer from the initial reference temperature  $T_0$ ;  $C_{ijkl}^{(n)}$  are the elastic constants of the  $n$ th layer;  $e_{ijk}^{(n)}$  are the piezoelectric constants of the  $n$ th layer;  $\gamma_{ij}^{(n)}$  are the thermal stress coefficients of the  $n$ th layer;  $\epsilon_{ij}^{(n)}$  are the dielectric constants of the  $n$ th layer;  $r_i^{(n)}$  are the pyroelectric constants of the  $n$ th layer;  $\chi^{(n)}$  is the entropy-temperature coefficient of the  $n$ th layer defined as

$$\chi^{(n)} = \rho^{(n)} c_v^{(n)} / T_0, \quad (35)$$

where  $\rho^{(n)}$  and  $c_v^{(n)}$  are the mass density and the specific heat per unit mass of the  $n$ th layer at constant strain.

Substituting SaS distributions (26) into the enthalpy function<sup>65</sup> and taking into account Equation (13), we obtain

$$H = \frac{1}{2} \iint_{\Omega} \sum_n \sum_{i_n} \sum_{j_n} \Lambda^{(n)i_n j_n} \left[ (\boldsymbol{\sigma}^{(n)i_n})^T \boldsymbol{\epsilon}^{(n)j_n} - (\mathbf{D}^{(n)i_n})^T \mathbf{E}^{(n)j_n} - S^{(n)i_n} \Theta^{(n)i_n} \right] A_1 A_2 d\theta_1 d\theta_2. \quad (36)$$

The use of constitutive equations (31)–(33) in (36) leads to the final form of enthalpy in terms of SaS variables

$$H = \iint_{\Omega} \sum_n \sum_{i_n} \sum_{j_n} \Lambda^{(n)i_n j_n} \left[ \frac{1}{2} (\boldsymbol{\epsilon}^{(n)i_n})^T \mathbf{C}^{(n)} \boldsymbol{\epsilon}^{(n)j_n} - (\mathbf{E}^{(n)i_n})^T \mathbf{e}^{(n)} \boldsymbol{\epsilon}^{(n)j_n} - \frac{1}{2} (\mathbf{E}^{(n)i_n})^T \boldsymbol{\epsilon}^{(n)} \mathbf{E}^{(n)j_n} \right. \\ \left. - (\boldsymbol{\epsilon}^{(n)i_n})^T \boldsymbol{\gamma}^{(n)} \Theta^{(n)j_n} - (\mathbf{E}^{(n)i_n})^T \mathbf{r}^{(n)} \Theta^{(n)j_n} - \frac{1}{2} \Theta^{(n)i_n} \chi^{(n)} \Theta^{(n)j_n} \right] A_1 A_2 d\theta_1 d\theta_2. \quad (37)$$

## 5 | HYBRID-MIXED THERMOPIEZOELECTRIC SOLID-SHELL ELEMENT

To develop the hybrid-mixed piezoelectric solid-shell element formulation, we introduce the displacement-independent strains  $\eta_{ij}^{(n)}$  and assume that they are distributed through the shell thickness according to the displacement-dependent strain distribution (26):

$$\eta_{ij}^{(n)} = \sum_{i_n} L^{(n)i_n} \eta_{ij}^{(n)i_n}, \quad (38)$$

where  $\eta_{ij}^{(n)i_n}$  are the displacement-independent strains of SaS of the  $n$ th layer.

Using Equations (26), (37), and (38) in the Hu–Washizu variational principle of thermopiezoelectricity,<sup>49</sup> in which displacements, strains, stresses and electric potential are utilized as independent variables, the following variational equation is obtained:

$$\delta \iint_{\Omega} \sum_n \sum_{i_n} \sum_{j_n} \Lambda^{(n)i_n j_n} \left[ \frac{1}{2} (\boldsymbol{\eta}^{(n)i_n})^T \mathbf{C}^{(n)} \boldsymbol{\eta}^{(n)j_n} - (\mathbf{E}^{(n)i_n})^T \mathbf{e}^{(n)} \boldsymbol{\eta}^{(n)j_n} - \frac{1}{2} (\mathbf{E}^{(n)i_n})^T \boldsymbol{\epsilon}^{(n)} \mathbf{E}^{(n)j_n} \right. \\ \left. - (\boldsymbol{\eta}^{(n)i_n})^T \boldsymbol{\gamma}^{(n)} \Theta^{(n)j_n} - (\mathbf{E}^{(n)i_n})^T \mathbf{r}^{(n)} \Theta^{(n)j_n} - \frac{1}{2} \Theta^{(n)i_n} \chi^{(n)} \Theta^{(n)j_n} - (\boldsymbol{\sigma}^{(n)i_n})^T (\boldsymbol{\eta}^{(n)j_n} - \boldsymbol{\epsilon}^{(n)j_n}) \right] A_1 A_2 d\theta_1 d\theta_2 = \delta W, \quad (39)$$

where  $\boldsymbol{\eta}^{(n)i_n} = [\eta_{11}^{(n)i_n} \eta_{22}^{(n)i_n} \eta_{33}^{(n)i_n} 2\eta_{12}^{(n)i_n} 2\eta_{13}^{(n)i_n} 2\eta_{23}^{(n)i_n}]^T$  are the displacement-independent strain vectors of SaS of the  $n$ th layer;  $W$  is the work done by external electromechanical loads:

$$W = \iint_{\Omega} \left( (\mathbf{u}^{[N]})^T \hat{\boldsymbol{\sigma}}^+ + \varphi^{[N]} \hat{D}_3^+ \right) A_1 A_2 c_1^+ c_2^+ d\theta_1 d\theta_2 - \iint_{\Omega} \left( (\mathbf{u}^{[0]})^T \hat{\boldsymbol{\sigma}}^- + \varphi^{[0]} \hat{D}_3^- \right) A_1 A_2 c_1^- c_2^- d\theta_1 d\theta_2 + W_{\Sigma}, \quad (40)$$

where  $\mathbf{u}^{[0]} = [u_1^{[0]} u_2^{[0]} u_3^{[0]}]^T$  and  $\mathbf{u}^{[N]} = [u_1^{[N]} u_2^{[N]} u_3^{[N]}]^T$  are the displacements vectors of the bottom and top surfaces;  $\varphi^{[0]}$  and  $\varphi^{[N]}$  are the electric potentials of the outer surfaces;  $c_{\alpha}^-$  and  $c_{\alpha}^+$  are the components of the shifter tensor on the outer surfaces introduced in Section 3;  $\hat{\boldsymbol{\sigma}}^- = [\hat{\sigma}_{13}^- \hat{\sigma}_{23}^- \hat{\sigma}_{33}^-]^T$  and  $\hat{\boldsymbol{\sigma}}^+ = [\hat{\sigma}_{13}^+ \hat{\sigma}_{23}^+ \hat{\sigma}_{33}^+]^T$  are the prescribed stresses acting on the outer surfaces;  $\hat{D}_3^-$  and  $\hat{D}_3^+$  are the prescribed electric displacements on the outer surfaces;  $W_{\Sigma}$  is the work done by electromechanical loads applied to the edge surface  $\Sigma$ .

The finite element formulation is based on a simple interpolation of displacements and electric potentials of SaS of the  $n$ th layer by a GeX four-node solid-shell element<sup>52,60</sup>

$$u_i^{(n)i_n} = \sum_r N_r u_{ir}^{(n)i_n}, \quad (41)$$

$$\varphi_r^{(n)i_n} = \sum_r N_r \varphi_r^{(n)i_n}, \quad (42)$$

where  $u_{ir}^{(n)i_n}$  and  $\varphi_r^{(n)i_n}$  are the displacements and electric potentials of SaS of the  $n$ th layer at element nodes;  $\xi_1$  and  $\xi_2$  are the normalized curvilinear coordinates  $\theta_1$  and  $\theta_2$  depicted in Figure 2; the nodal index  $r$  runs from 1 to 4.

To implement analytical integration throughout the solid-shell element, the extended ANS method<sup>52</sup> is used to interpolate displacements of SaS of the  $n$ th layer

$$\boldsymbol{\varepsilon}^{(n)i_n} = \sum_r N_r \boldsymbol{\varepsilon}_r^{(n)i_n}, \quad (43)$$

where  $\boldsymbol{\varepsilon}_r^{(n)i_n} = [\varepsilon_{11r}^{(n)i_n} \varepsilon_{22r}^{(n)i_n} \varepsilon_{33r}^{(n)i_n} 2\varepsilon_{12r}^{(n)i_n} 2\varepsilon_{13r}^{(n)i_n} 2\varepsilon_{23r}^{(n)i_n}]^T$  are the displacement-dependent strain vectors of SaS of the  $n$ th layer at element nodes, which are evaluated as

$$\boldsymbol{\varepsilon}_r^{(n)i_n} = \mathbf{B}_{ur}^{(n)i_n} \mathbf{q}, \quad (44)$$

where  $\mathbf{B}_{ur}^{(n)i_n}$  are the *constant* matrices of order  $6 \times 12N_{\text{SaS}}$  presented in Reference 52;  $\mathbf{q}$  is the displacement vector of the solid-shell element given by

$$\mathbf{q} = [\mathbf{q}_1^T \mathbf{q}_2^T \mathbf{q}_3^T \mathbf{q}_4^T]^T, \quad (45)$$

$$\mathbf{q}_r = \left[ (\mathbf{u}_r^{[0]})^T (\mathbf{u}_r^{(1)2})^T \dots (\mathbf{u}_r^{(1)I_1-1})^T (\mathbf{u}_r^{[1]})^T (\mathbf{u}_r^{(2)2})^T \dots (\mathbf{u}_r^{(N-1)I_{N-1}-1})^T (\mathbf{u}_r^{[N-1]})^T (\mathbf{u}_r^{(N)2})^T \dots (\mathbf{u}_r^{(N)I_N-1})^T (\mathbf{u}_r^{[N]})^T \right]^T, \\ \mathbf{u}_r^{[m]} = [u_{1r}^{[m]} u_{2r}^{[m]} u_{3r}^{[m]}]^T, \quad \mathbf{u}_r^{(n)m_n} = [u_{1r}^{(n)m_n} u_{2r}^{(n)m_n} u_{3r}^{(n)m_n}]^T,$$

where  $u_{ir}^{[0]}$  and  $u_{ir}^{[N]}$  are the displacements of the outer surfaces at element nodes;  $u_{ir}^{[m]}$  and  $u_{ir}^{(n)m_n}$  are the displacements of interfaces and inner SaS of the  $n$ th layer at element nodes.

The extended ANS method<sup>60</sup> can be also applied to interpolate the electric field of SaS of the  $n$ th layer

$$\mathbf{E}_r^{(n)i_n} = \sum_r N_r \mathbf{E}_r^{(n)i_n}, \quad (46)$$

where  $\mathbf{E}_r^{(n)i_n} = [E_{1r}^{(n)i_n} E_{2r}^{(n)i_n} E_{3r}^{(n)i_n}]^T$  are the electric field vectors of SaS of the  $n$ th layer at element nodes defined as

$$\mathbf{E}_r^{(n)i_n} = -\mathbf{B}_{\varphi r}^{(n)i_n} \Phi, \quad (47)$$

where  $\mathbf{B}_{\varphi_r}^{(n)i_n}$  are the *constant* matrices of order  $3 \times 4N_{\text{SaS}}$  given in Appendix B;  $\Phi$  is the electric potential vector of the solid-shell element:

$$\Phi = [\Phi_1^T \Phi_2^T \Phi_3^T \Phi_4^T]^T, \quad (48)$$

$$\Phi_r = \left[ \varphi_r^{[0]} \varphi_r^{(1)2} \dots \varphi_r^{(1)I_1-1} \varphi_r^{[1]} \varphi_r^{(2)2} \dots \varphi_r^{(N-1)I_{N-1}-1} \varphi_r^{[N-1]} \varphi_r^{(N)2} \dots \varphi_r^{(N)I_N-1} \varphi_r^{[N]} \right]^T,$$

where  $\varphi_r^{[0]}$  and  $\varphi_r^{[N]}$  are the nodal electric potentials on the outer surfaces;  $\varphi_r^{[m]}$  and  $\varphi_r^{(n)m_n}$  are the electric potentials on interfaces and inner SaS of the  $n$ th layer at element nodes.

The extended ANS interpolations (43) and (46) can be written in a more convenient form as

$$\mathbf{e}^{(n)i_n} = \sum_{r_1, r_2} (\xi_1)^{r_1} (\xi_2)^{r_2} \mathbf{B}_{ur_1 r_2}^{(n)i_n} \mathbf{q}, \quad (49)$$

$$\mathbf{E}^{(n)i_n} = - \sum_{r_1, r_2} (\xi_1)^{r_1} (\xi_2)^{r_2} \mathbf{B}_{\varphi r_1 r_2}^{(n)i_n} \Phi, \quad (50)$$

where  $\mathbf{B}_{ur_1 r_2}^{(n)i_n}$  are the matrices of order  $6 \times 12N_{\text{SaS}}$  and  $\mathbf{B}_{\varphi r_1 r_2}^{(n)i_n}$  are the matrices of order  $3 \times 4N_{\text{SaS}}$  given by

$$\mathbf{B}_{ur_1 r_2}^{(n)i_n} = \frac{1}{4} \left[ \mathbf{B}_{u1}^{(n)i_n} + (1 - 2r_1) \mathbf{B}_{u2}^{(n)i_n} + (1 - 2r_1)(1 - 2r_2) \mathbf{B}_{u3}^{(n)i_n} + (1 - 2r_2) \mathbf{B}_{u4}^{(n)i_n} \right], \quad (51)$$

$$\mathbf{B}_{\varphi r_1 r_2}^{(n)i_n} = \frac{1}{4} \left[ \mathbf{B}_{\varphi 1}^{(n)i_n} + (1 - 2r_1) \mathbf{B}_{\varphi 2}^{(n)i_n} + (1 - 2r_1)(1 - 2r_2) \mathbf{B}_{\varphi 3}^{(n)i_n} + (1 - 2r_2) \mathbf{B}_{\varphi 4}^{(n)i_n} \right]. \quad (52)$$

Here and in the following developments, the indices  $r_1$  and  $r_2$  run from 0 to 1.

The similar interpolation is used for the temperature field:

$$\Theta^{(n)i_n} = \sum_{r_1, r_2} (\xi_1)^{r_1} (\xi_2)^{r_2} \Theta_{r_1 r_2}^{(n)i_n}, \quad (53)$$

$$\Theta_{r_1 r_2}^{(n)i_n} = \frac{1}{4} \left[ \Theta_1^{(n)i_n} + (1 - 2r_1) \Theta_2^{(n)i_n} + (1 - 2r_1)(1 - 2r_2) \Theta_3^{(n)i_n} + (1 - 2r_2) \Theta_4^{(n)i_n} \right], \quad (54)$$

where  $\Theta_r^{(n)i_n}$  is the temperature rise of the SaS of the  $n$ th layer at element nodes.

To circumvent shear and membrane locking and avoid spurious zero energy modes, the assumed interpolation of stresses<sup>52</sup> is employed

$$\boldsymbol{\sigma}^{(n)i_n} = \sum_{r_1+r_2 < 2} (\xi_1)^{r_1} (\xi_2)^{r_2} \mathbf{Q}_{r_1 r_2} \boldsymbol{\sigma}_{r_1 r_2}^{(n)i_n}, \quad (55)$$

$$\boldsymbol{\sigma}_{00}^{(n)i_n} = \left[ \mu_1^{(n)i_n} \mu_2^{(n)i_n} \mu_3^{(n)i_n} \mu_4^{(n)i_n} \mu_5^{(n)i_n} \mu_6^{(n)i_n} \right]^T,$$

$$\boldsymbol{\sigma}_{01}^{(n)i_n} = \left[ \mu_7^{(n)i_n} \mu_9^{(n)i_n} \mu_{11}^{(n)i_n} \right]^T, \quad \boldsymbol{\sigma}_{10}^{(n)i_n} = \left[ \mu_8^{(n)i_n} \mu_{10}^{(n)i_n} \mu_{12}^{(n)i_n} \right]^T,$$

where  $\mathbf{Q}_{r_1 r_2}$  are the projective matrices given by

$$\mathbf{Q}_{00} = \begin{bmatrix} 1 & 0 & 0 & 0 & 0 & 0 \\ 0 & 1 & 0 & 0 & 0 & 0 \\ 0 & 0 & 1 & 0 & 0 & 0 \\ 0 & 0 & 0 & 1 & 0 & 0 \\ 0 & 0 & 0 & 0 & 1 & 0 \\ 0 & 0 & 0 & 0 & 0 & 1 \end{bmatrix}, \quad \mathbf{Q}_{01} = \begin{bmatrix} 1 & 0 & 0 \\ 0 & 0 & 0 \\ 0 & 1 & 0 \\ 0 & 0 & 0 \\ 0 & 0 & 1 \\ 0 & 0 & 0 \end{bmatrix}, \quad \mathbf{Q}_{10} = \begin{bmatrix} 0 & 0 & 0 \\ 1 & 0 & 0 \\ 0 & 1 & 0 \\ 0 & 0 & 0 \\ 0 & 0 & 0 \\ 0 & 0 & 1 \end{bmatrix}. \quad (56)$$

The displacement-independent strains are interpolated in the same way

$$\begin{aligned}\boldsymbol{\eta}^{(n)i_n} &= \sum_{r_1+r_2<2} (\xi_1)^{r_1} (\xi_2)^{r_2} \mathbf{Q}_{r_1 r_2} \boldsymbol{\eta}_{r_1 r_2}^{(n)i_n}, & (57) \\ \boldsymbol{\eta}_{00}^{(n)i_n} &= \left[ \psi_1^{(n)i_n} \psi_2^{(n)i_n} \psi_3^{(n)i_n} \psi_4^{(n)i_n} \psi_5^{(n)i_n} \psi_6^{(n)i_n} \right]^T, \\ \boldsymbol{\eta}_{01}^{(n)i_n} &= \left[ \psi_7^{(n)i_n} \psi_9^{(n)i_n} \psi_{11}^{(n)i_n} \right]^T, \quad \boldsymbol{\eta}_{10}^{(n)i_n} = \left[ \psi_8^{(n)i_n} \psi_{10}^{(n)i_n} \psi_{12}^{(n)i_n} \right]^T,\end{aligned}$$

Due to interpolation (57), we introduce 12 strain parameters  $\psi_1^{(n)i_n}, \psi_2^{(n)i_n}, \dots, \psi_{12}^{(n)i_n}$  for each SaS, that is,  $12N_{\text{SaS}}$  for all SaS. This seems excessive for a SaS-based four-node solid-shell element with  $12N_{\text{SaS}}$  displacement DOF. However, there exist six dependent strain modes, which provide a correct rank of the element stiffness matrix in the purely mechanical solid-shell element formulation.<sup>61</sup> In the electromechanical SaS-based solid-shell element formulation, there are exactly seven zero energy modes, namely six modes related to the rigid-body motions and one to the short circuit.<sup>61</sup> All other deformation modes are associated with nonzero eigenvalues.

Substituting interpolations (41), (42), (49), (50), (53), (55), and (57) into the Hu–Washizu variational equation (39) and (40), and replacing the metric product  $A_1 A_2$  and components of the shifter tensor in surface integrals by their values at the element center, we can analytically integrate throughout the element. Taking into account the fact that  $\det [\Lambda^{(n)i_n j_n}] \neq 0$  for each layer,<sup>52</sup> the following equilibrium equations of the GeX SaS-based hybrid-mixed thermopiezoelectric solid-shell element are obtained:

$$\boldsymbol{\eta}_{r_1 r_2}^{(n)i_n} = \mathbf{Q}_{r_1 r_2}^T \mathbf{B}_{ur_1 r_2}^{(n)i_n} \mathbf{q} \text{ for } r_1 + r_2 < 2, \quad (58)$$

$$\boldsymbol{\sigma}_{r_1 r_2}^{(n)i_n} = \mathbf{Q}_{r_1 r_2}^T \left( \mathbf{C}^{(n)} \mathbf{Q}_{r_1 r_2} \boldsymbol{\eta}_{r_1 r_2}^{(n)i_n} + (\mathbf{e}^{(n)})^T \mathbf{B}_{\varphi r_1 r_2}^{(n)i_n} \boldsymbol{\Phi} - \boldsymbol{\gamma}^{(n)} \Theta_{r_1 r_2}^{(n)i_n} \right) \text{ for } r_1 + r_2 < 2, \quad (59)$$

$$\sum_n \sum_{i_n} \sum_{j_n} \Lambda^{(n)i_n j_n} \sum_{r_1+r_2<2} \frac{1}{3^{r_1+r_2}} \left( \mathbf{B}_{ur_1 r_2}^{(n)i_n} \right)^T \mathbf{Q}_{r_1 r_2} \boldsymbol{\sigma}_{r_1 r_2}^{(n)j_n} = \mathbf{F}_u, \quad (60)$$

$$\begin{aligned} & \sum_n \sum_{i_n} \sum_{j_n} \Lambda^{(n)i_n j_n} \left[ \sum_{r_1+r_2<2} \frac{1}{3^{r_1+r_2}} \left( \mathbf{B}_{\varphi r_1 r_2}^{(n)i_n} \right)^T \mathbf{e}^{(n)} \mathbf{Q}_{r_1 r_2} \boldsymbol{\eta}_{r_1 r_2}^{(n)j_n} \right. \\ & \left. - \sum_{r_1+r_2 \leq 2} \frac{1}{3^{r_1+r_2}} \left( \mathbf{B}_{\varphi r_1 r_2}^{(n)i_n} \right)^T \left( \boldsymbol{\epsilon}^{(n)} \mathbf{B}_{\varphi r_1 r_2}^{(n)j_n} \boldsymbol{\Phi} - \mathbf{r}^{(n)} \Theta_{r_1 r_2}^{(n)j_n} \right) \right] = \mathbf{F}_\varphi, \end{aligned} \quad (61)$$

where  $\mathbf{F}_u$  and  $\mathbf{F}_\varphi$  are the mechanical and electric surface vectors of the element given in Appendix B.

*Remark.* To calculate the weighted coefficients  $\Lambda^{(n)i_n j_n}$ , we employ the  $(I_n + 1)$ -point Gaussian quadrature rule to fulfill exact integration in Equation (13). This is sufficient because  $L^{(n)i_n}$  are the Lagrange basis polynomials of degree  $I_n - 1$  and  $c_\alpha$  are the first degree polynomials.

Eliminating stress and strain vectors  $\boldsymbol{\sigma}_{r_1 r_2}^{(n)i_n}$  and  $\boldsymbol{\eta}_{r_1 r_2}^{(n)i_n}$  from Equations (58)–(61) at the element level, we arrive at the system of algebraic equations

$$\begin{bmatrix} \mathbf{K}_{uu} & \mathbf{K}_{u\varphi} \\ \mathbf{K}_{\varphi u} & \mathbf{K}_{\varphi\varphi} \end{bmatrix} \begin{bmatrix} \mathbf{q} \\ \boldsymbol{\Phi} \end{bmatrix} = \begin{bmatrix} \mathbf{F}_u + \mathbf{F}_{u\theta} \\ \mathbf{F}_\varphi + \mathbf{F}_{\varphi\theta} \end{bmatrix}, \quad (62)$$

where  $\mathbf{K}_{uu}, \mathbf{K}_{u\varphi}, \mathbf{K}_{\varphi u} = \mathbf{K}_{u\varphi}^T$  and  $\mathbf{K}_{\varphi\varphi}$  are the mechanical, piezoelectric, and dielectric stiffness matrices;  $\mathbf{F}_{u\theta}$  and  $\mathbf{F}_{\varphi\theta}$  are the thermal expansion and pyroelectric vectors of the solid-shell element defined as

$$\mathbf{K}_{uu} = \sum_n \sum_{i_n} \sum_{j_n} \Lambda^{(n)i_n j_n} \sum_{r_1+r_2<2} \frac{1}{3^{r_1+r_2}} \left( \mathbf{B}_{ur_1 r_2}^{(n)i_n} \right)^T \mathbf{Q}_{r_1 r_2} \mathbf{Q}_{r_1 r_2}^T \mathbf{C}^{(n)} \mathbf{Q}_{r_1 r_2} \mathbf{Q}_{r_1 r_2}^T \mathbf{B}_{ur_1 r_2}^{(n)j_n}, \quad (63)$$

$$\mathbf{K}_{u\varphi} = \sum_n \sum_{i_n} \sum_{j_n} \Lambda^{(n)i_n j_n} \sum_{r_1+r_2<2} \frac{1}{3^{r_1+r_2}} \left( \mathbf{B}_{ur_1 r_2}^{(n)i_n} \right)^T \mathbf{Q}_{r_1 r_2} \mathbf{Q}_{r_1 r_2}^T (\mathbf{e}^{(n)})^T \mathbf{B}_{\varphi r_1 r_2}^{(n)j_n}, \quad (64)$$

$$\mathbf{K}_{\varphi\varphi} = - \sum_n \sum_{i_n} \sum_{j_n} \Lambda^{(n)i_n j_n} \sum_{r_1+r_2 \leq 2} \frac{1}{3^{r_1+r_2}} \left( \mathbf{B}_{\varphi r_1 r_2}^{(n)i_n} \right)^T \boldsymbol{\epsilon}^{(n)} \mathbf{B}_{\varphi r_1 r_2}^{(n)j_n}, \quad (65)$$

$$\mathbf{F}_{u\theta} = \sum_n \sum_{i_n} \sum_{j_n} \Lambda^{(n)i_n j_n} \sum_{r_1+r_2 \leq 2} \frac{1}{3^{r_1+r_2}} \left( \mathbf{B}_{ur_1 r_2}^{(n)i_n} \right)^T \mathbf{Q}_{r_1 r_2} \mathbf{Q}_{r_1 r_2}^T \boldsymbol{\gamma}^{(n)} \Theta_{r_1 r_2}^{(n)j_n}, \quad (66)$$

$$\mathbf{F}_{\varphi\theta} = - \sum_n \sum_{i_n} \sum_{j_n} \Lambda^{(n)i_n j_n} \sum_{r_1+r_2 \leq 2} \frac{1}{3^{r_1+r_2}} \left( \mathbf{B}_{\varphi r_1 r_2}^{(n)i_n} \right)^T \mathbf{r}^{(n)} \Theta_{r_1 r_2}^{(n)j_n}. \quad (67)$$

## 6 | NUMERICAL EXAMPLES

The developed GeXSaS4 piezoelectric solid-shell element is evaluated using exact solutions extracted from the literature and authors' examples as well to demonstrate its ability to analyze the coupled thermo-electro-mechanical fields in thick and thin laminated piezoelectric shell structures with particular attention to the 3D stress analysis.

### 6.1 | Simply supported four-layer cylindrical shell under temperature loading

Here, we study a two-layer antisymmetric angle-ply cylindrical shell [45/−45] composed of the graphite/epoxy composite and covered with PZT-5A layers on its bottom and top surfaces. This means that the hybrid four-layer cylindrical shell [PZT5A/45/−45/PZT5A] with ply thicknesses [0.25  $h$ /0.25  $h$ /0.25  $h$ /0.25  $h$ ] is considered. The boundary conditions for the simply supported shell with electrically grounded edges maintained at the reference temperature are written as

$$\Theta^{(n)} = \varphi^{(n)} = \sigma_{11}^{(n)} = \sigma_{12}^{(n)} = u_3^{(n)} = 0 \text{ at } \theta_1 = 0 \text{ and } \theta_1 = L, \quad (68)$$

where  $\theta_1$  is the axial coordinate;  $L$  is the length of the shell;  $n = 1, 2, 3, 4$ . The cylindrical shell is subjected to sinusoidally distributed temperature loading on the top surface, while the bottom surface is maintained at the reference temperature. The boundary conditions on the bottom and top surfaces are expressed as follows:

$$\begin{aligned} \Theta^- &= D_3^- = \sigma_{13}^- = \sigma_{23}^- = \sigma_{33}^- = 0, \\ \Theta^+ &= \Theta_0 \sin \frac{\pi \theta_1}{L}, \quad D_3^+ = \sigma_{13}^+ = \sigma_{23}^+ = \sigma_{33}^+ = 0, \end{aligned} \quad (69)$$

where  $\Theta_0 = 1$  K. It is assumed that both interfaces between the piezoelectric layers and the composite shell are grounded. The mechanical properties of the PZT-5A<sup>10</sup> are

$$\begin{aligned} C_{1111} &= C_{2222} = 99.201 \text{ GPa}, \quad C_{3333} = 86.856 \text{ GPa}, \quad C_{1122} = 54.016 \text{ GPa}, \\ C_{1133} &= C_{2233} = 50.778 \text{ GPa}, \quad C_{1313} = C_{2323} = 21.1 \text{ GPa}, \quad C_{1212} = 22.593 \text{ GPa}, \\ \gamma_{11} &= \gamma_{22} = 3.314 \times 10^5 \text{ Pa/K}, \quad \gamma_{33} = 3.26 \times 10^5 \text{ Pa/K}, \quad \kappa_{11} = \kappa_{22} = \kappa_{33} = 1.8 \text{ W/mK}, \\ e_{311} &= e_{322} = -7.209 \text{ C/m}^2, \quad e_{333} = 15.118 \text{ C/m}^2, \quad e_{113} = e_{223} = 12.322 \text{ C/m}^2, \\ \epsilon_{11} &= \epsilon_{22} = 1.53 \times 10^{-8} \text{ F/m}, \quad \epsilon_{33} = 1.5 \times 10^{-8} \text{ F/m}, \quad r_3 = 7.0 \times 10^{-4} \text{ C/m}^2\text{K}. \end{aligned}$$

The material properties of the graphite-epoxy composite<sup>18</sup> are

$$\begin{aligned} E_L &= 172.5 \text{ GPa}, \quad E_T = 6.9 \text{ GPa}, \quad G_{LT} = 3.45 \text{ GPa}, \quad G_{TT} = 1.38 \text{ GPa}, \quad \nu_{LT} = \nu_{TT} = 0.25, \\ \alpha_L &= 0.57 \times 10^{-6} \text{ 1/K}, \quad \alpha_T = 35.6 \times 10^{-6} \text{ 1/K}, \quad \kappa_L = 36.42 \text{ W/mK}, \quad \kappa_T = 0.96 \text{ W/mK}, \\ \epsilon_L &= 3.095 \times 10^{-11} \text{ F/m}, \quad \epsilon_T = 2.653 \times 10^{-11} \text{ F/m}, \end{aligned}$$

where  $E_L$ ,  $E_T$ ,  $G_{LT}$  and  $G_{TT}$  are the elastic moduli;  $\nu_{LT}$  and  $\nu_{TT}$  are the Poisson's ratios;  $\alpha_L$  and  $\alpha_T$  are the coefficients of thermal expansion; L and T indicate fiber and transverse directions.

To compare the results with the exact SaS-based solution,<sup>22</sup> we introduce dimensionless variables at crucial points as follows:

$$\begin{aligned}\bar{\Theta} &= \Theta(L/2, z) / \Theta_0, \quad \bar{q}_3 = 100hq_3(L/2, z) / \kappa_r \Theta_0, \\ \bar{\varphi} &= 10^3 d_r \varphi(L/2, z) / h \alpha_r \Theta_0, \quad \bar{D}_3 = 10^3 SD_3(L/2, z) / E_r d_r \alpha_r \Theta_0, \\ \bar{u}_1 &= 100u_1(0, z) / R \alpha_r \Theta_0, \quad \bar{u}_2 = 100u_2(0, z) / R \alpha_r \Theta_0, \\ \bar{u}_3 &= 10u_3(L/2, z) / R \alpha_r \Theta_0, \quad \bar{\sigma}_{11} = \sigma_{11}(L/2, z) / E_r \alpha_r \Theta_0, \\ \bar{\sigma}_{22} &= \sigma_{22}(L/2, z) / E_r \alpha_r \Theta_0, \quad \bar{\sigma}_{13} = 10S\sigma_{13}(0, z) / E_r \alpha_r \Theta_0, \\ \bar{\sigma}_{23} &= 10S\sigma_{23}(0, z) / E_r \alpha_r \Theta_0, \quad \bar{\sigma}_{33} = 10S\sigma_{33}(L/2, z) / E_r \alpha_r \Theta_0, \quad z = \theta_3/h,\end{aligned}$$

where  $E_r = 6.9$  GPa,  $\alpha_r = 35.6 \times 10^{-6}$  1/K,  $\kappa_r = 36.42$  W/mK, and  $d_r = 374 \times 10^{-12}$  m/V are the representative moduli;  $S = R/h$  is the slenderness ratio. The geometric parameters of the shell are taken to be  $L = 4$  m and  $R = 1$  m, where  $R$  is the radius of the middle surface.

Due to symmetry of the problem, one half of the shell ( $0 \leq \theta_1 \leq L/2$ ) with the following boundary conditions:

$$\begin{aligned}\Theta^{(n)}(0) &= \varphi^{(n)}(0) = u_3^{(n)}(0) = 0, \\ u_1^{(n)}(L/2) &= u_2^{(n)}(L/2) = 0\end{aligned}\quad (70)$$

is modeled by regular meshes of axisymmetric GeXSaS4 elements. Tables 1 and 2 list the results of the convergence study due to mesh refinement for thick and moderately thick cylindrical shells using seven SaS for each layer. The obtained results are compared with the exact SaS-based solution<sup>22</sup> using the same number of SaS. Additionally, Figure 3 shows the results of the convergence study for different slenderness ratios including thin shells with  $S = 100$  and 1000. The analytical answer is provided by the exact solution.<sup>22</sup> It is seen that the GeXSaS4 element behaves very well even for coarse meshes. Figures 4 and 5 display the distributions of temperature, electric potential, displacements, heat flux, electric displacement and stresses using five SaS for each layer and 256 elements compared with the exact solution.<sup>22</sup> These results demonstrate convincingly the high potential of the proposed GeX SaS-based hybrid-mixed solid-shell element formulation. This is because of the fact that the boundary conditions on the bottom and top surfaces and the continuity conditions on the interfaces for the transverse components of the stress tensor and the electric displacement vector are satisfied for thick and thin shells properly.

## 6.2 | Simply supported piezoelectric cylindrical panel under heat flux loading

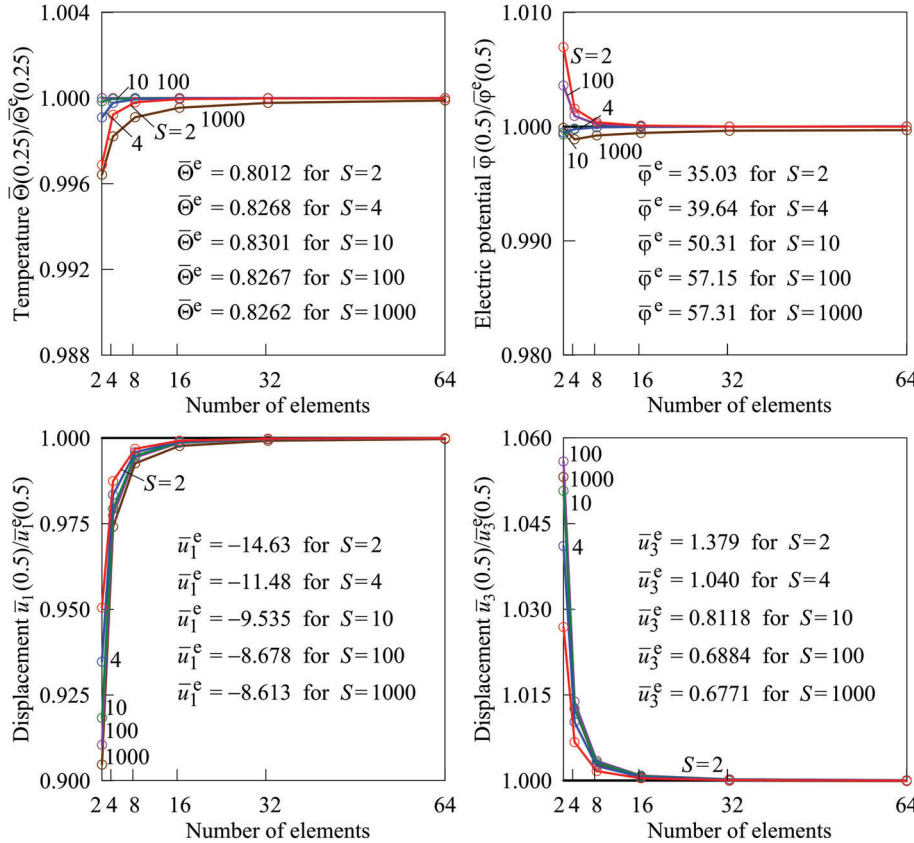
Consider a piezoceramic cylindrical panel composed of the PZT-5A with the material properties presented in the previous section. The boundary conditions for the simply supported cylindrical panel with electrically grounded edges maintained at the reference temperature can be written as

**TABLE 1** Convergence study for a hybrid four-layer cylindrical shell with  $R/h = 2$  using seven sampling surfaces for each layer

Number of elements	$\bar{\Theta}$ (0.25)	$\bar{q}_3$ (0.375)	$\bar{\varphi}$ (0.5)	$\bar{D}_3$ (0.375)	$\bar{u}_1$ (0.5)	$\bar{u}_2$ (0.5)	$\bar{u}_3$ (0.5)	$\bar{\sigma}_{11}$ (0.5)	$\bar{\sigma}_{22}$ (0.5)	$\bar{\sigma}_{13}$ (0.125)	$\bar{\sigma}_{23}$ (0.125)	$\bar{\sigma}_{33}$ (0.125)
16	0.80115	-3.9763	35.029	25.462	-14.619	-8.5813	1.3793	-1.3501	-1.4143	-1.6691	-0.59156	1.6498
64	0.80120	-3.9252	35.026	16.555	-14.630	-8.5865	1.3788	-1.3537	-1.3838	-1.6725	-0.56996	1.6355
256	0.80120	-3.9257	35.026	16.583	-14.631	-8.5868	1.3788	-1.3538	-1.3840	-1.6727	-0.57009	1.6357
Exact	0.80120	-3.9257	35.026	16.583	-14.631	-8.5869	1.3788	-1.3538	-1.3840	-1.6727	-0.57009	1.6357

**TABLE 2** Convergence study for a hybrid four-layer cylindrical shell with  $R/h = 10$  using seven sampling surfaces for each layer

Number of elements	$\bar{\Theta}(0.25)$	$\bar{q}_3(0.375)$	$\bar{\varphi}(0.5)$	$\bar{D}_3(0.375)$	$\bar{u}_1(0.5)$	$\bar{u}_2(0.5)$	$\bar{u}_3(0.5)$	$\bar{\sigma}_{11}(0.5)$	$\bar{\sigma}_{22}(0.5)$	$\bar{\sigma}_{13}(0.125)$	$\bar{\sigma}_{23}(0.125)$	$\bar{\sigma}_{33}(0.125)$
16	0.83003	-3.4027	50.311	35.960	-9.5225	-1.5452	0.81243	-2.0229	-2.0457	-3.1551	-0.91505	3.8510
64	0.83005	-3.3592	50.312	6.0975	-9.5344	-1.5462	0.81185	-2.0276	-2.0117	-3.1560	-0.87724	3.8328
256	0.83005	-3.3597	50.312	6.2066	-9.5352	-1.5463	0.81182	-2.0279	-2.0120	-3.1603	-0.87745	3.8333
Exact	0.83005	-3.3597	50.312	6.2011	-9.5352	-1.5463	0.81181	-2.0279	-2.0120	-3.1603	-0.87745	3.8333

**FIGURE 3** Convergence study due to mesh refinement for a four-layer cylindrical shell using five SaS for each layer: reference values are provided by the exact SaS-based solution<sup>22</sup> using seven SaS

$$\begin{aligned}
 \Theta^{(n)} = \varphi^{(n)} = \sigma_{11}^{(n)} = u_2^{(n)} = u_3^{(n)} = 0 \quad \text{at } \theta_1 = 0 \text{ and } \theta_1 = a, \\
 \Theta^{(n)} = \varphi^{(n)} = u_1^{(n)} = \sigma_{22}^{(n)} = u_3^{(n)} = 0 \quad \text{at } \theta_2 = 0 \text{ and } \theta_2 = b,
 \end{aligned} \tag{71}$$

where  $\theta_1$  and  $\theta_2$  are the axial and circumferential coordinates;  $a$  is the length of the panel;  $b = \phi R$  is the length of the circular arc;  $\phi$  is the arc angle and  $n = 1$ . The shell is loaded on the top surface by a sinusoidally distributed heat flux, whereas the bottom surface is heat-insulating. The boundary conditions on the bottom and top surfaces are

$$\begin{aligned}
 q_3^- = D_3^- = \sigma_{13}^- = \sigma_{23}^- = \sigma_{33}^- = 0, \\
 q_3^+ = q_0 \sin \frac{\pi \theta_1}{a} \sin \frac{\pi \theta_2}{b}, \quad D_3^+ = \sigma_{13}^+ = \sigma_{23}^+ = \sigma_{33}^+ = 0,
 \end{aligned} \tag{72}$$

where  $q_0 = 1 \text{ W/m}^2$ . The geometric parameters of the shell are chosen to be  $R = 1 \text{ m}$ ,  $a = 4 \text{ m}$ , and  $b = \pi/2 \text{ m}$ .

To compare the results with the exact SaS-based solution,<sup>22</sup> we introduce dimensionless variables at crucial points as functions of the thickness coordinate  $z = \theta_3/h$  as

**FIGURE 4** Through-thickness distributions of temperature, electric potential and displacements for a four-layer cylindrical shell using 256 elements and five SaS for each layer compared with the exact solution<sup>22</sup> using seven SaS (○)

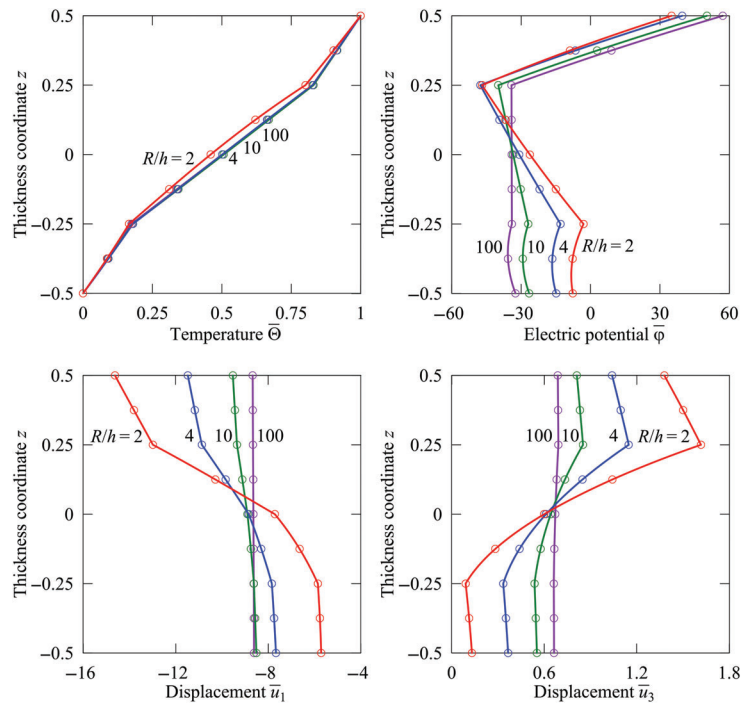
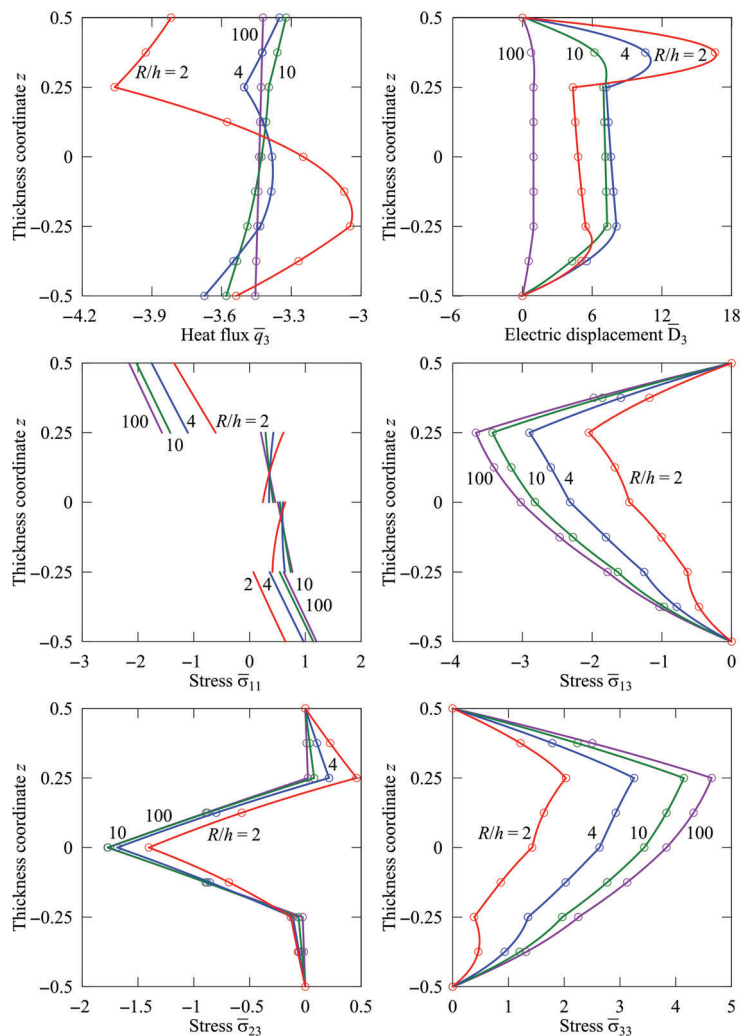


**FIGURE 5** Through-thickness distributions of heat flux, electric displacement and stresses for a four-layer cylindrical shell using 256 elements and five SaS for each layer compared with the exact solution<sup>22</sup> using seven SaS (○)





$$\bar{\Theta} = 10\kappa_r\Theta(a/2, b/2, z)/SRq_0, \quad \bar{q}_3 = q_3(a/2, b/2, z)/q_0,$$

$$\bar{\varphi} = \kappa_r d_r \varphi(a/2, b/2, z)/R^2 \alpha_r q_0, \quad \bar{D}_3 = \kappa_r SD_3(a/2, b/2, z)/RE_r d_r \alpha_r q_0,$$

$$\bar{u}_1 = \kappa_r u_1(0, b/2, z)/SR^2 \alpha_r q_0, \quad \bar{u}_2 = \kappa_r u_2(a/2, 0, z)/SR^2 \alpha_r q_0,$$

$$\bar{u}_3 = \kappa_r u_3(a/2, b/2, z)/SR^2 \alpha_r q_0, \quad \bar{\sigma}_{11} = \kappa_r \sigma_{11}(a/2, b/2, z)/RE_r \alpha_r q_0,$$

$$\bar{\sigma}_{22} = \kappa_r \sigma_{22}(a/2, b/2, z)/RE_r \alpha_r q_0, \quad \bar{\sigma}_{13} = \kappa_r \sigma_{13}(0, b/2, z)/RE_r \alpha_r q_0,$$

$$\bar{\sigma}_{23} = \kappa_r \sigma_{23}(a/2, 0, z)/RE_r \alpha_r q_0, \quad \bar{\sigma}_{33} = \kappa_r \sigma_{33}(a/2, b/2, z)/RE_r \alpha_r q_0,$$

where  $E_r = 10.3$  GPa,  $\alpha_r = 1.5 \times 10^{-6}$  1/K,  $\kappa_r = 1.8$  W/mK, and  $d_r = 374 \times 10^{-12}$  m/V are the representative moduli;  $S = R/h$  is the slenderness ratio.

Due to symmetry of the problem, one quarter of the shell ( $0 \leq \theta_1 \leq a/2$ ,  $0 \leq \theta_2 \leq b/2$ ) is discretized by regular meshes shown in Figure 6. Tables 3 and 4 list the results of the convergence study due to mesh refinement for thick and moderately thick cylindrical panels compared with the exact SaS-based solution.<sup>22</sup> The results of the convergence study for different slenderness ratios using five SaS and regular  $k \times k$  meshes with the mesh parameter  $k = 2, 4, 8, 16, 32$  and  $64$  are presented in Figure 7. The reference values are provided by Reference 22 using seven SaS. It is seen that the GeXSaS4

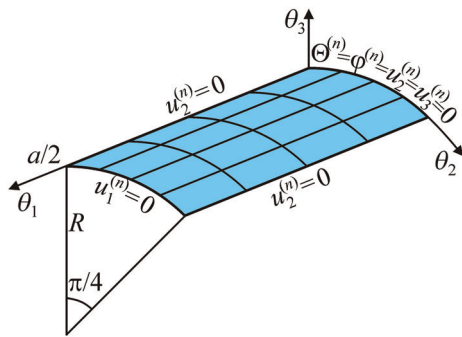


FIGURE 6 One quarter of the cylindrical panel modeled by  $4 \times 4$  mesh

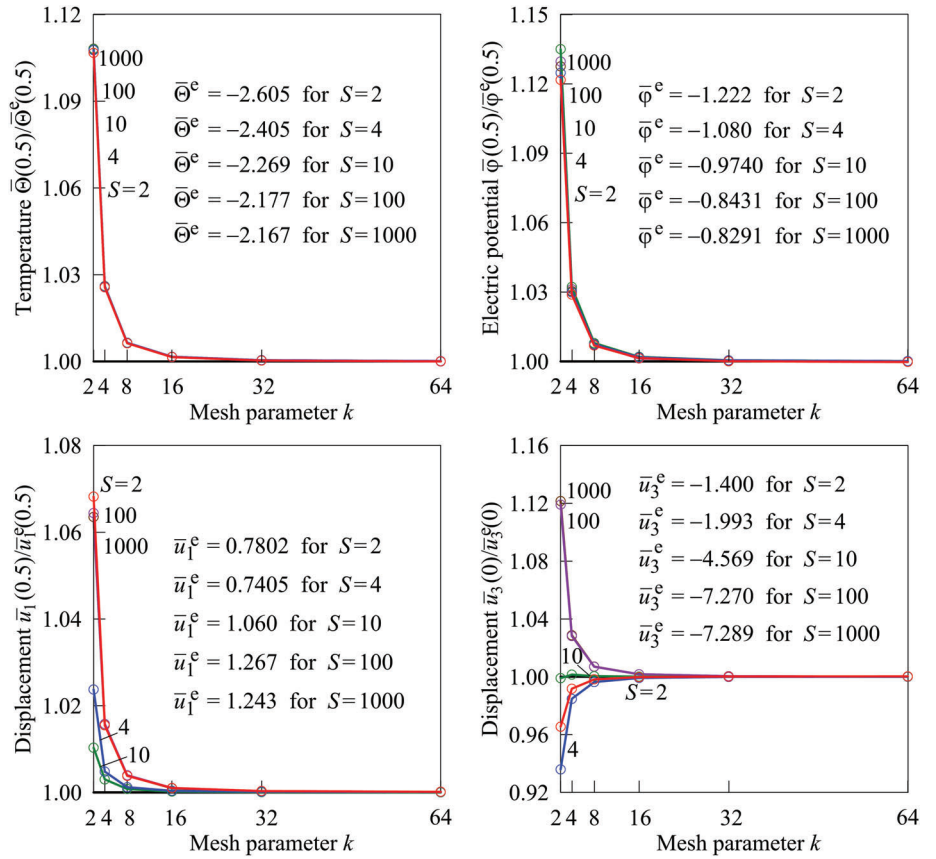
TABLE 3 Convergence study for a piezoelectric cylindrical panel with  $R/h = 4$  using seven sampling surfaces

Mesh	$\bar{\Theta}(0)$	$\bar{q}_3(0)$	$\bar{\varphi}(0.5)$	$\bar{D}_3(0)$	$\bar{u}_1(0.5)$	$\bar{u}_2(0.5)$	$\bar{u}_3(0)$	$\bar{\sigma}_{11}(0.5)$	$\bar{\sigma}_{22}(0.5)$	$\bar{\sigma}_{13}(0)$	$\bar{\sigma}_{23}(0)$	$\bar{\sigma}_{33}(0)$
$4 \times 4$	-2.4678	1.0909	-1.1121	-45.088	0.74397	0.14724	-1.9619	10.507	-8.4638	-0.91354	-4.3622	8.8847
$16 \times 16$	-2.4093	0.57555	-1.0818	-17.960	0.74069	0.11028	-1.9907	10.767	-10.496	-0.97364	-2.3390	1.0864
$64 \times 64$	-2.4057	0.56839	-1.0799	-17.584	0.74050	0.10796	-1.9925	10.791	-10.556	-0.97763	-2.3118	0.97666
$128 \times 128$	-2.4055	0.56834	-1.0798	-17.580	0.74049	0.10785	-1.9926	10.792	-10.558	-0.97784	-2.3117	0.97620
Exact	-2.4055	0.56834	-1.0798	-17.575	0.74049	0.10781	-1.9926	10.788	-10.563	-0.97777	-2.3114	0.97613

TABLE 4 Convergence study for a piezoelectric cylindrical panel with  $R/h = 10$  using seven sampling surfaces

Mesh	$\bar{\Theta}(0)$	$\bar{q}_3(0)$	$\bar{\varphi}(0.5)$	$\bar{D}_3(0)$	$\bar{u}_1(0.5)$	$\bar{u}_2(0.5)$	$\bar{u}_3(0)$	$\bar{\sigma}_{11}(0.5)$	$\bar{\sigma}_{22}(0.5)$	$\bar{\sigma}_{13}(0)$	$\bar{\sigma}_{23}(0)$	$\bar{\sigma}_{33}(0)$
$4 \times 4$	-2.3278	1.0207	-1.0053	-146.80	1.0629	-1.3054	-4.5759	-8.1928	-50.633	-1.1892	-5.6695	32.176
$16 \times 16$	-2.2724	0.53834	-0.97589	-18.153	1.0599	-1.3462	-4.5695	-8.7253	-47.246	-1.2328	-2.9716	1.7949
$64 \times 64$	-2.2690	0.53164	-0.97408	-16.277	1.0597	-1.3487	-4.5689	-8.7439	-47.272	-1.2357	-2.9329	1.3403
$128 \times 128$	-2.2689	0.53159	-0.97399	-16.261	1.0597	-1.3488	-4.5689	-8.7447	-47.276	-1.2359	-2.9325	1.3366
Exact	-2.2688	0.53159	-0.97396	-16.261	1.0597	-1.3488	-4.5689	-8.7447	-47.276	-1.2359	-2.9324	1.3366

**FIGURE 7** Convergence study due to mesh refinement for a cylindrical panel using five SaS and regular meshes  $k \times k$ : reference values are provided by the exact SaS-based solution<sup>22</sup> using seven SaS



element behaves well for coarse meshes. Figures 8 and 9 display the through-thickness distributions of temperature, electric potential, displacements, heat flux, electric displacement, and stresses using a fine  $128 \times 128$  mesh and five SaS for  $S = 100$ , and seven SaS for  $S = 2, 4, \text{ and } 10$  compared with the exact solution.<sup>22</sup> As can be seen, the boundary conditions on the bottom and top surfaces for the transverse stresses and electric displacement are satisfied again with a very high accuracy.

### 6.3 | Piezoelectric spherical shell under axisymmetric thermal loading

Next, we study a piezoceramic spherical shell made of the PZT-5A with the material properties given in Section 6.1. The coefficients of the first and second fundamental forms, and Christoffel symbols of the spherical surface with holes at the poles are defined as

$$\begin{aligned} A_1 &= R, & A_2 &= R \sin \theta_1, & k_1 &= 1/R, & k_2 &= 1/R, \\ B_1 &= 0, & B_2 &= \frac{\cos \theta_1}{R \sin \theta_1}, & \theta_1 &\in [\vartheta, \pi - \vartheta] \end{aligned} \quad (73)$$

that can be readily found using the mapping of the rectangle in  $(\theta_1, \theta_2)$ -space into a spherical surface in  $(x_1, x_2, x_3)$ -space given by

$$x_1 = R \sin \theta_1 \cos \theta_2, \quad x_2 = R \sin \theta_1 \sin \theta_2, \quad x_3 = R \cos \theta_1, \quad (74)$$

where  $R$  is the radius of the middle surface;  $\theta_1$  and  $\theta_2$  are the meridional and circumferential coordinates of the middle surface. The angle  $\vartheta = 0.001^\circ$  is chosen small that allows us to avoid singularity.

Axisymmetric convective boundary conditions on the inner and outer surfaces<sup>14</sup> are written as

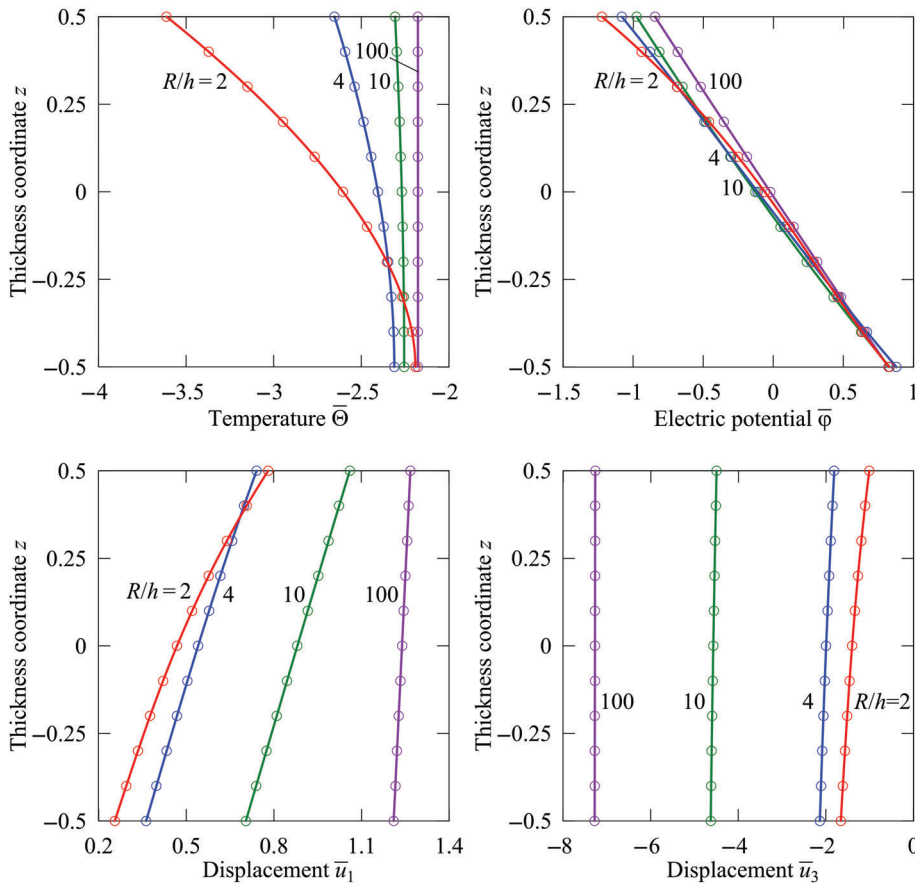


**FIGURE 8** Through-thickness distributions of temperature, electric potential and displacements for a cylindrical panel using  $128 \times 128$  mesh with five SaS for  $S = 100$  and seven SaS for  $S = 2, 4$ , and  $10$  compared with the exact solution<sup>22</sup> using 11 SaS (○)

$$\begin{aligned} \Theta_{,3}^{(n)}(-h/2) - \alpha^- \Theta^- &= 0, & \varphi^- &= \sigma_{33}^- = 0, \\ \Theta_{,3}^{(n)}(h/2) + \alpha^+ \Theta^+ &= \alpha^+ \Theta_0, & \varphi^+ &= \sigma_{33}^+ = 0, \end{aligned} \quad (75)$$

where  $\alpha^- = h^-/\kappa_{33}$ ,  $\alpha^+ = h^+/\kappa_{33}$ ,  $\Theta_0 = 1$  K,  $h\alpha^- = 0.2$ ,  $h\alpha^+ = 2$ , and  $n = 1$ .

Owing to symmetry, one sixteenth of the shell is discretized by regular meshes shown in Figure 10. To compare the results with the exact solution of thermopiezoelectricity (see Appendix C), we introduce dimensionless variables at point  $P(\pi/4, 0)$  belonging to the middle surface as functions of the dimensionless thickness coordinate as follows:

$$\bar{\Theta} = \Theta(P, z)/\Theta_0, \quad \bar{q}_3 = 100hq_3(P, z)/\kappa_r\Theta_0,$$

$$\bar{\varphi} = 10d_r\varphi(P, z)/h\alpha_r\Theta_0, \quad \bar{D}_3 = D_3(P, z)/10E_r d_r\alpha_r\Theta_0, \quad \bar{u}_3 = 10u_3(P, z)/R\alpha_r\Theta_0,$$

$$\bar{\sigma}_{11} = \sigma_{11}(P, z)/E_r\alpha_r\Theta_0, \quad \bar{\sigma}_{33} = R\sigma_{33}(P, z)/hE_r\alpha_r\Theta_0, \quad z = \theta_3/h,$$

where  $E_r = 10.3$  GPa,  $\alpha_r = 1.5 \times 10^{-6}$  1/K,  $\kappa_r = 1.8$  W/mK, and  $d_r = 374 \times 10^{-12}$  m/V are the representative moduli and  $R = 1$  m.

Tables 5 and 6 list the results of the convergence study due to increasing a number of SaS for thick and thin spherical shells using  $128 \times 1$  mesh. As can be seen, the developed piezoelectric solid-shell element provides four right digits for the fundamental variables using nine and five SaS for thick and thin shells, respectively. Figure 11 shows the through-thickness distributions of temperature, heat flux, electric potential, electric displacement, transverse displacement, and transverse normal stress using nine SaS and the same mesh. It is seen that the boundary conditions on the inner and outer surfaces for the transverse normal stress are satisfied very well for thick and thin shells.

**FIGURE 9** Through-thickness distributions of heat flux, electric displacement and stresses for a cylindrical panel using  $128 \times 128$  mesh with five SaS for  $S = 100$  and seven SaS for  $S = 2, 4,$  and  $10$  compared with the exact solution<sup>22</sup> using 11 SaS (○)

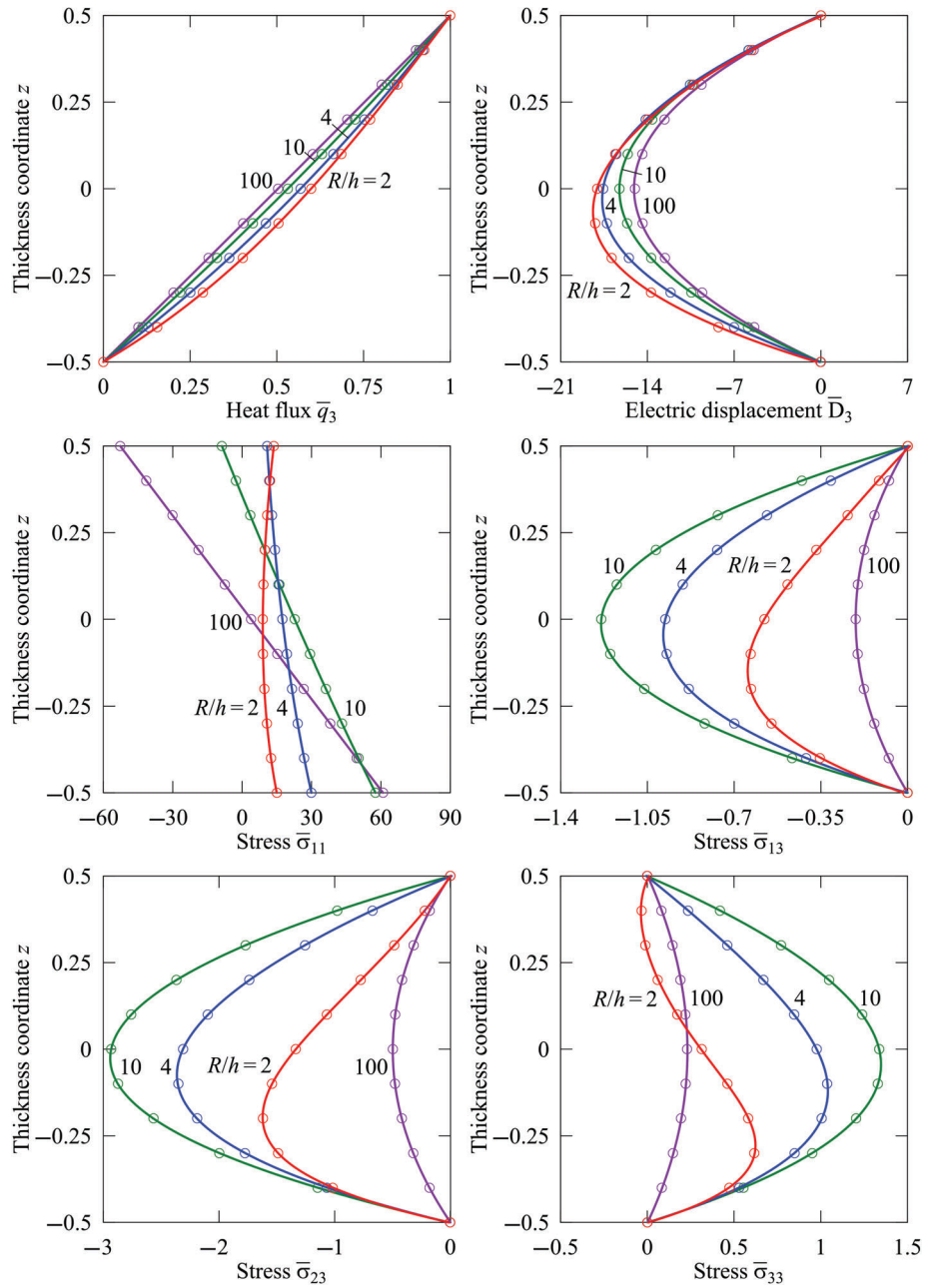
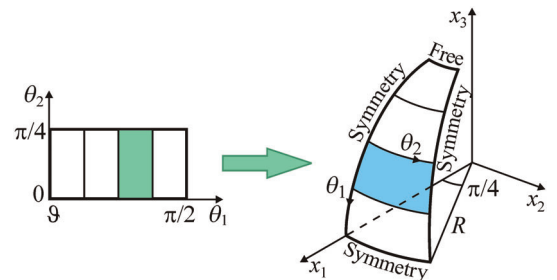


**FIGURE 10** One sixteenth of the spherical shell modeled by  $4 \times 1$  mesh



Number of sampling surfaces	$\bar{\Theta}(0)$	$\bar{q}_3(0)$	$\bar{\varphi}(0)$	$\bar{D}_3(0)$	$\bar{u}_3(0)$	$\bar{\sigma}_{11}(-0.5)$	$\bar{\sigma}_{33}(0)$
3	0.9296	-10.35	-12.20	11.54	10.09	16.82	9.077
5	0.9299	-9.717	-12.72	10.80	10.18	22.82	10.27
7	0.9299	-9.735	-12.72	10.82	10.16	23.43	10.06
9	0.9299	-9.734	-12.72	10.82	10.16	23.39	10.04
Exact solution	0.9299	-9.732	-12.72	10.82	10.16	23.39	10.04

**TABLE 5** Convergence study for the piezoelectric spherical shell with  $R/h = 2$  using  $128 \times 1$  mesh

Number of sampling surfaces	$\bar{\Theta}(0)$	$\bar{q}_3(0)$	$\bar{\varphi}(0)$	$\bar{D}_3(0)$	$\bar{u}_3(0)$	$\bar{\sigma}_{11}(-0.5)$	$\bar{\sigma}_{33}(0)$
3	0.8484	-15.28	-2.254	10.40	8.486	4.446	1.402
5	0.8484	-15.28	-2.254	10.40	8.486	4.451	2.219
Exact solution	0.8484	-15.28	-2.254	10.40	8.486	4.451	2.219

**TABLE 6** Convergence study for the piezoelectric spherical shell with  $R/h = 100$  using  $128 \times 1$  mesh

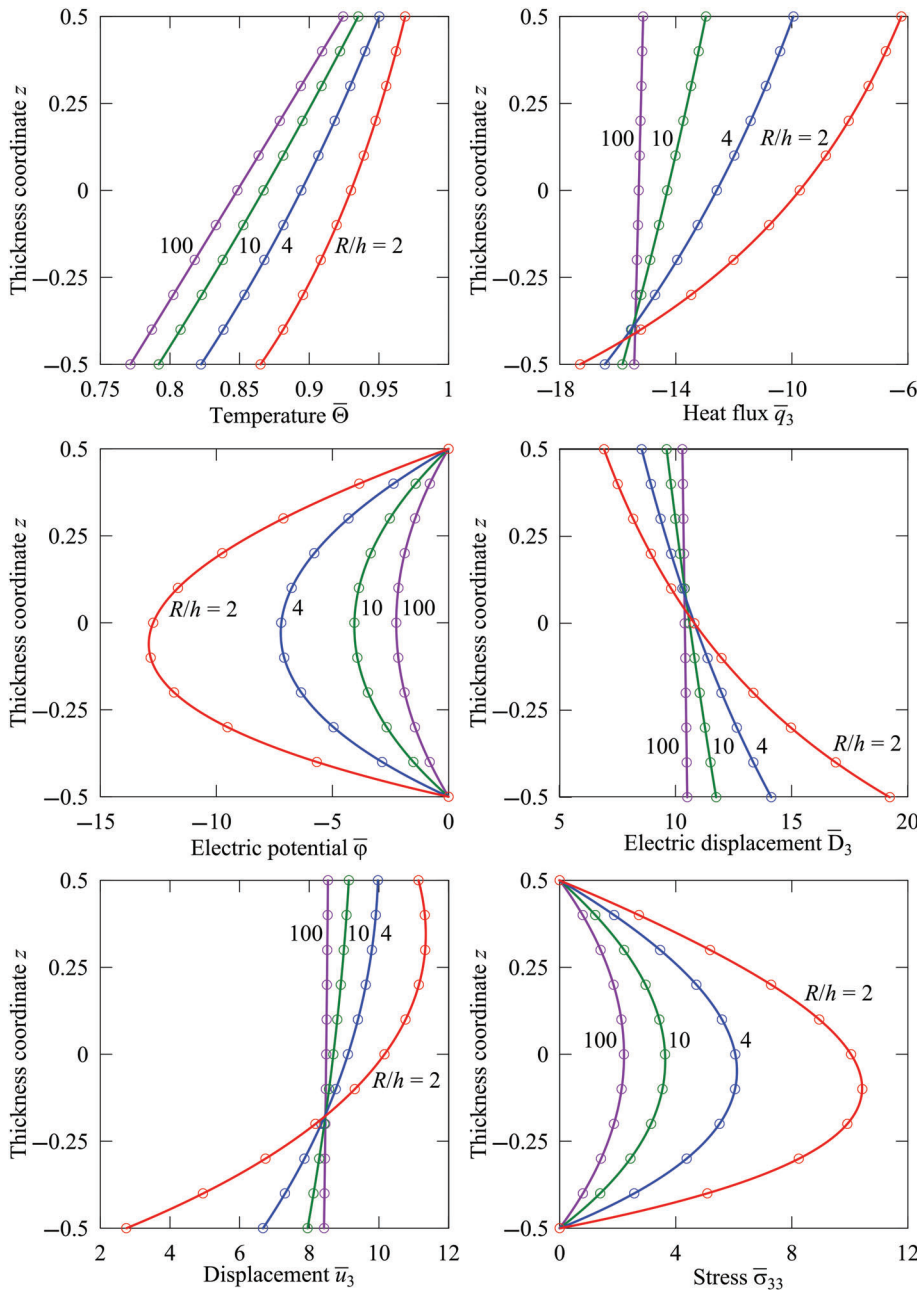


**FIGURE 11** Through-thickness distributions of temperature, heat flux, electric potential, electric displacement, transverse displacement and transverse normal stress for the axisymmetric spherical shell at point  $P(\pi/4, 0)$  using nine SaS and  $128 \times 1$  mesh compared with the exact solution of thermopiezoelectricity (○)

## 6.4 | Piezoelectric spherical shell under general thermal load conditions

Let us consider more general thermal loading of the piezoceramic spherical shell with small holes at the poles ( $\vartheta = 0.001^\circ$ ) analyzed in the previous section. The asymmetric convective boundary conditions on the inner and outer surfaces are

$$\begin{aligned} \Theta_{,3}^{(n)}(-h/2) - \alpha^- \Theta^- &= 0, \quad \varphi^- = \sigma_{13}^- = \sigma_{23}^- = \sigma_{33}^- = 0, \\ \Theta_{,3}^{(n)}(h/2) + \alpha^+ \Theta^+ &= \alpha^+ \Theta_0 \theta_1 (\pi - \theta_1) \sin^2(2\theta_2), \quad \varphi^+ = \sigma_{13}^+ = \sigma_{23}^+ = \sigma_{33}^+ = 0, \end{aligned} \quad (76)$$

where  $\Theta_0 = 1 \text{ K}$ ,  $h\alpha^- = 0.2$ ,  $h\alpha^+ = 2$ , and  $n = 1$ .

Due to symmetry of the problem, we consider only one sixteenth of the spherical shell (Figure 10). To analyze the obtained results, we utilize dimensionless variables from the previous section at point  $P(\pi/2, \pi/4)$  belonging to the middle surface and introduce additional variables

$$\bar{\sigma}_{22} = \sigma_{22}(P, z) / E_r \alpha_r \Theta_0, \quad \bar{\sigma}_{13} = 100R\sigma_{13}(P, z) / hE_r \alpha_r \Theta_0, \quad \bar{\sigma}_{23} = 100R\sigma_{23}(P, z) / hE_r \alpha_r \Theta_0$$

as functions of the thickness coordinate  $z = \theta_3/h$ . Figure 12 shows the results of the convergence study for thick and thin shells using seven SaS and regular  $k \times k$  meshes with the mesh parameter  $k = 2, 4, 8, 16, 32$  and  $64$ . The reference values are provided by using seven SaS and  $96 \times 96$  mesh. It is seen that the GeXSaS4 element behaves very well for coarse meshes. Figures 13 and 14 display distributions of the temperature, heat flux, electric potential, electric displacement, transverse displacement, and stresses using seven SaS and  $96 \times 96$  mesh. It can be seen that the boundary conditions on the inner and outer surfaces for transverse stresses are again fulfilled correctly.

## 6.5 | Three-layer hyperbolic shell under thermal loading

Next, we study a two-layer composite hyperbolic shell with the PZT-5A layer attached to its upper surface. Therefore, the hybrid three-layer shell  $[0/90/\text{PZT5A}]$  with equal thicknesses is considered. The fibers of the lower and upper layers are oriented respectively in the meridional and circumferential directions. The interface between the shell and the piezoceramic layer is grounded. This problem allows us to test the proposed analytical integration schemes, since we deal here with a doubly-curved shell with variable coefficients of the first and second fundamental forms and Christoffel symbols of the middle surface:

$$\begin{aligned} A_1 &= \sqrt{1 + \frac{\tau^2 \theta_1^2}{\rho^2}}, \quad A_2 = \rho, \quad k_1 = -\frac{\tau r^2}{\rho^3 A_1^3}, \quad k_2 = \frac{1}{\rho A_1}, \\ B_1 &= 0, \quad B_2 = \frac{\tau \theta_1}{\rho^2 A_1}, \quad \theta_1 \in [-L, L], \quad \theta_2 \in [0, 2\pi], \end{aligned} \quad (77)$$

which are obtained using the mapping of the rectangle in  $(\theta_1, \theta_2)$ -space into a hyperbolic surface in  $(x_1, x_2, x_3)$ -space defined as

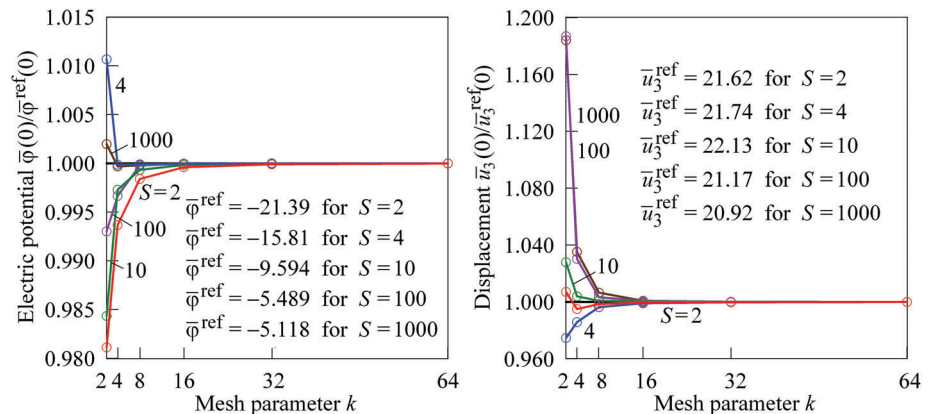


**FIGURE 12** Convergence study due to mesh refinement for the asymmetric spherical shell using seven SaS and regular meshes  $k \times k$ : reference values are provided by using seven SaS and  $96 \times 96$  mesh

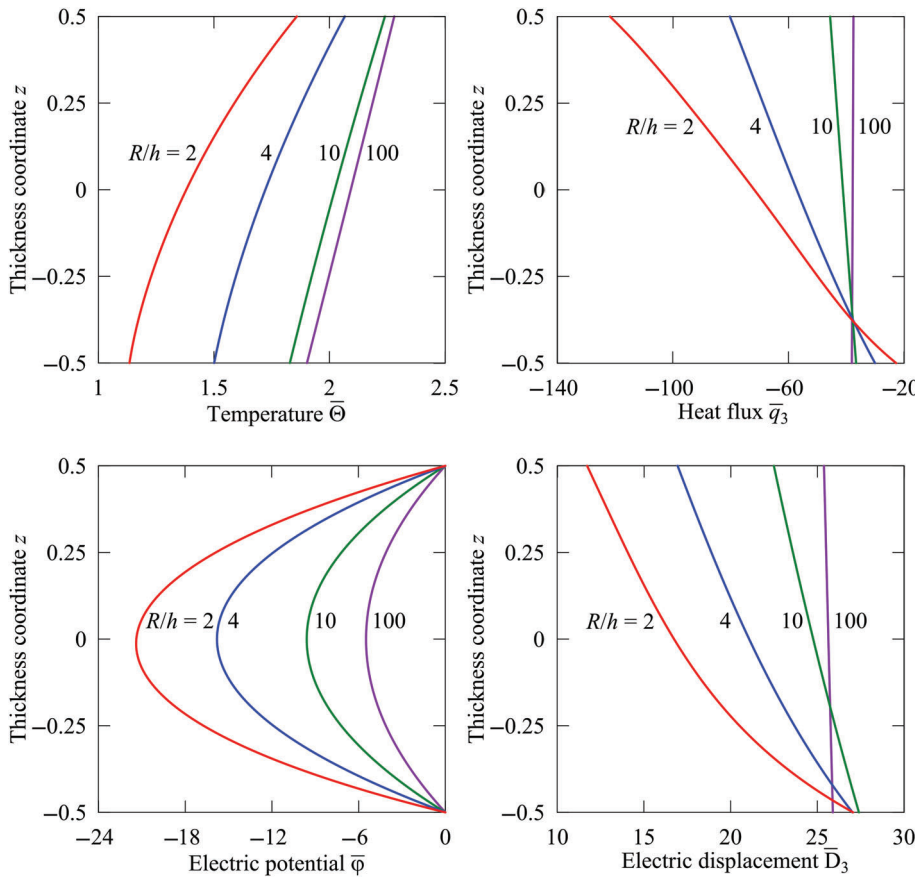


**FIGURE 13** Through-thickness distributions of temperature, heat flux, electric potential and electric displacement for the asymmetric spherical shell at point  $P(\pi/2, \pi/4)$  using seven SaS and  $96 \times 96$  mesh

$$\begin{aligned}
 x_1 &= \rho \sin \theta_2, & x_2 &= \rho \cos \theta_2, & x_3 &= \theta_1, \\
 \rho &= \sqrt{r^2 + \tau \theta_1^2}, & \tau &= (R^2 - r^2) / L^2,
 \end{aligned} \tag{78}$$

where  $2L$  is the length of the shell;  $r$  and  $R$  are the radii of the hyperbolic surface (see Figure 15);  $\theta_1$  and  $\theta_2$  are the meridional and circumferential coordinates of the middle surface.

The boundary conditions on the lower and upper surfaces are written as

$$\begin{aligned}
 \Theta^- &= \Theta_0 (1 - \theta_1^2 / L^2) \sin^2 \theta_2, & D_3^- &= \sigma_{13}^- = \sigma_{23}^- = \sigma_{33}^- = 0, \\
 \Theta^+ &= D_3^+ = \sigma_{13}^+ = \sigma_{23}^+ = \sigma_{33}^+ = 0,
 \end{aligned} \tag{79}$$

where  $\Theta_0 = 1$  K. The material properties of the graphite-epoxy composite and PZT-5A are presented in Section 6.1. The geometric parameters of a shell are  $L = 200$  mm,  $R = 150$  mm,  $r = 75$  mm, and  $h_1 = h_2 = h_3 = 2$  mm.

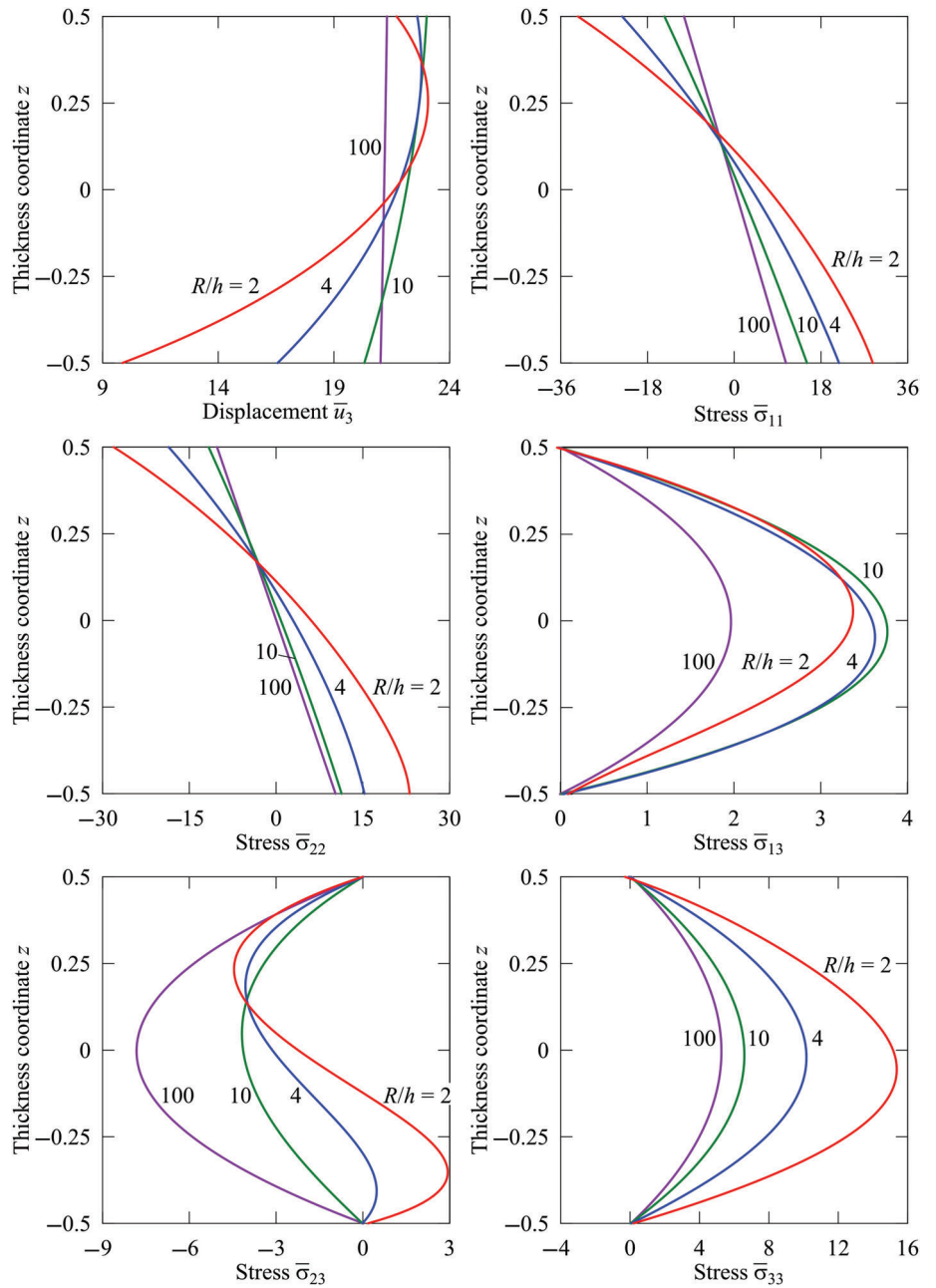
For convenience, we introduce dimensionless variables at any point  $P(\theta_1, \theta_2)$  belonging to the middle surface as functions of the thickness coordinate  $z = \theta_3/h$  as follows:

$$\begin{aligned}
 \bar{\Theta} &= \Theta(P, z) / \Theta_0, & \bar{\varphi} &= 10^3 d_r \varphi(P, z) / h \alpha_r \Theta_0, & \bar{D}_3 &= 10^3 D_3(P, z) / E_r d_r \alpha_r \Theta_0, \\
 \bar{u}_1 &= 100 u_1(P, z) / R \alpha_r \Theta_0, & \bar{u}_3 &= 10 u_3(P, z) / R \alpha_r \Theta_0, \\
 \bar{\sigma}_{13} &= 10^3 \sigma_{13}(P, z) / E_r \alpha_r \Theta_0, & \bar{\sigma}_{23} &= 10^3 \sigma_{23}(P, z) / E_r \alpha_r \Theta_0, & \bar{\sigma}_{33} &= 10^2 \sigma_{33}(P, z) / E_r \alpha_r \Theta_0,
 \end{aligned}$$

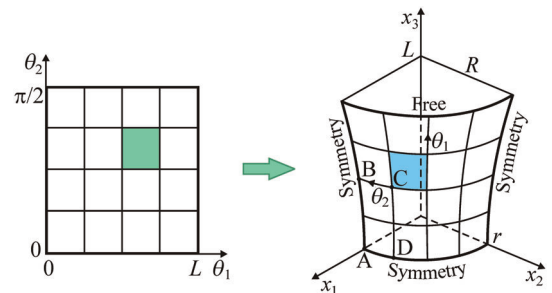
where  $E_r = 6.9$  GPa,  $\alpha_r = 35.6 \times 10^{-6}$  1/K and  $d_r = 374 \times 10^{-12}$  m/V are the representative moduli.

Owing to symmetry of the problem, only one octant of the shell is modeled by regular meshes (Figure 15). The results of the convergence study using five SaS for each layer and regular  $k \times k$  meshes with the mesh parameter  $k = 4, 8, 16, 32,$  and  $64$  are presented in Figure 16. Figure 17 shows the through-thickness distributions of temperature, electric potential, electric displacement and transverse stresses using five SaS for each layer and  $64 \times 64$  mesh. As can be

**FIGURE 14** Through-thickness distributions of transverse displacement and stresses for the asymmetric spherical shell at point  $P(\pi/2, \pi/4)$  using seven SaS and  $96 \times 96$  mesh



**FIGURE 15** One octant of the three-layer hyperbolic shell modeled by  $4 \times 4$  mesh





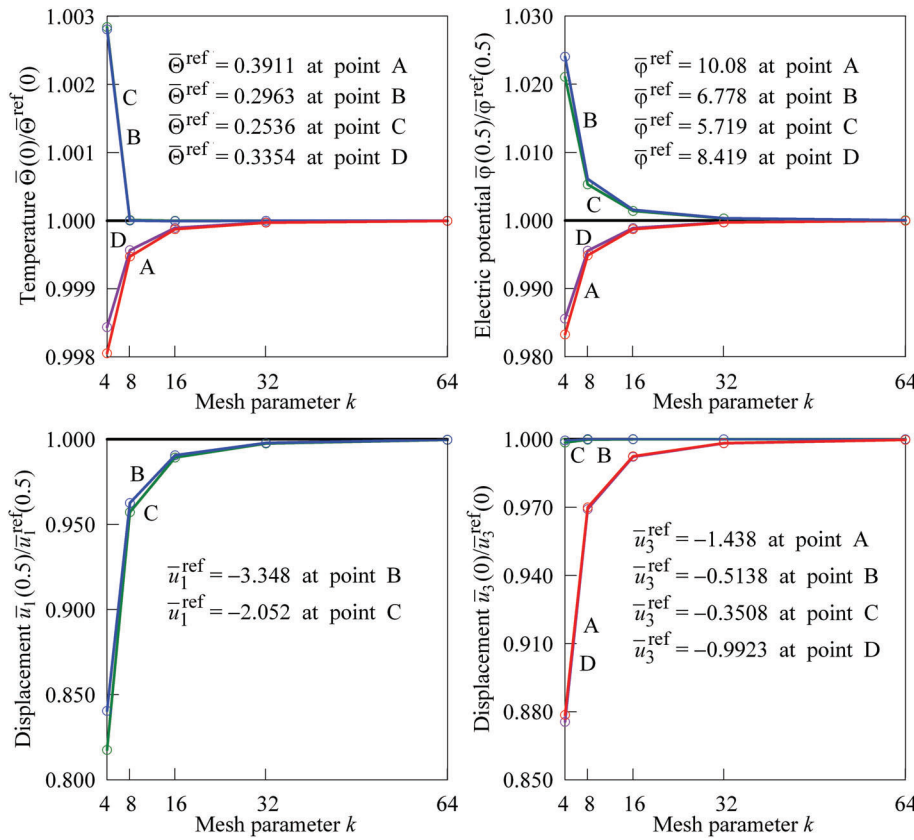


**FIGURE 16** Convergence study due to mesh refinement for a three-layer hyperbolic shell at points A( $0, \pi/2$ ), B( $L/2, \pi/2$ ), C( $L/2, 3\pi/8$ ), and D( $0, 3\pi/8$ ) using five SaS for each layer and regular meshes  $k \times k$ : reference values are provided by using five SaS and  $96 \times 96$  mesh

seen, the GeXSa4 element describes very well the boundary conditions on the lower and upper surfaces and the continuity conditions at the interfaces for the transverse components of the stress tensor and the electric displacement vector.

## 6.6 | Three-layer hyperbolic shell under combined thermal and electric loading

Finally, we study a two-layer composite hyperbolic shell with the PZT-5A layer attached to its upper surface considered in the previous section. The shell is subjected to combined thermal and electric loading as follows:

$$\begin{aligned} \Theta^- &= \Theta_0 (1 - \theta_1^2/L^2), & D_3^- &= \sigma_{13}^- = \sigma_{23}^- = \sigma_{33}^- = 0, \\ \varphi^+ &= \varphi_0 (1 - \theta_1^2/L^2), & \Theta^+ &= \sigma_{13}^+ = \sigma_{23}^+ = \sigma_{33}^+ = 0, \end{aligned} \quad (80)$$

where  $\Theta_0 = 1$  K,  $\varphi_0 = 0$  V,  $-10$  V and  $-20$  V.

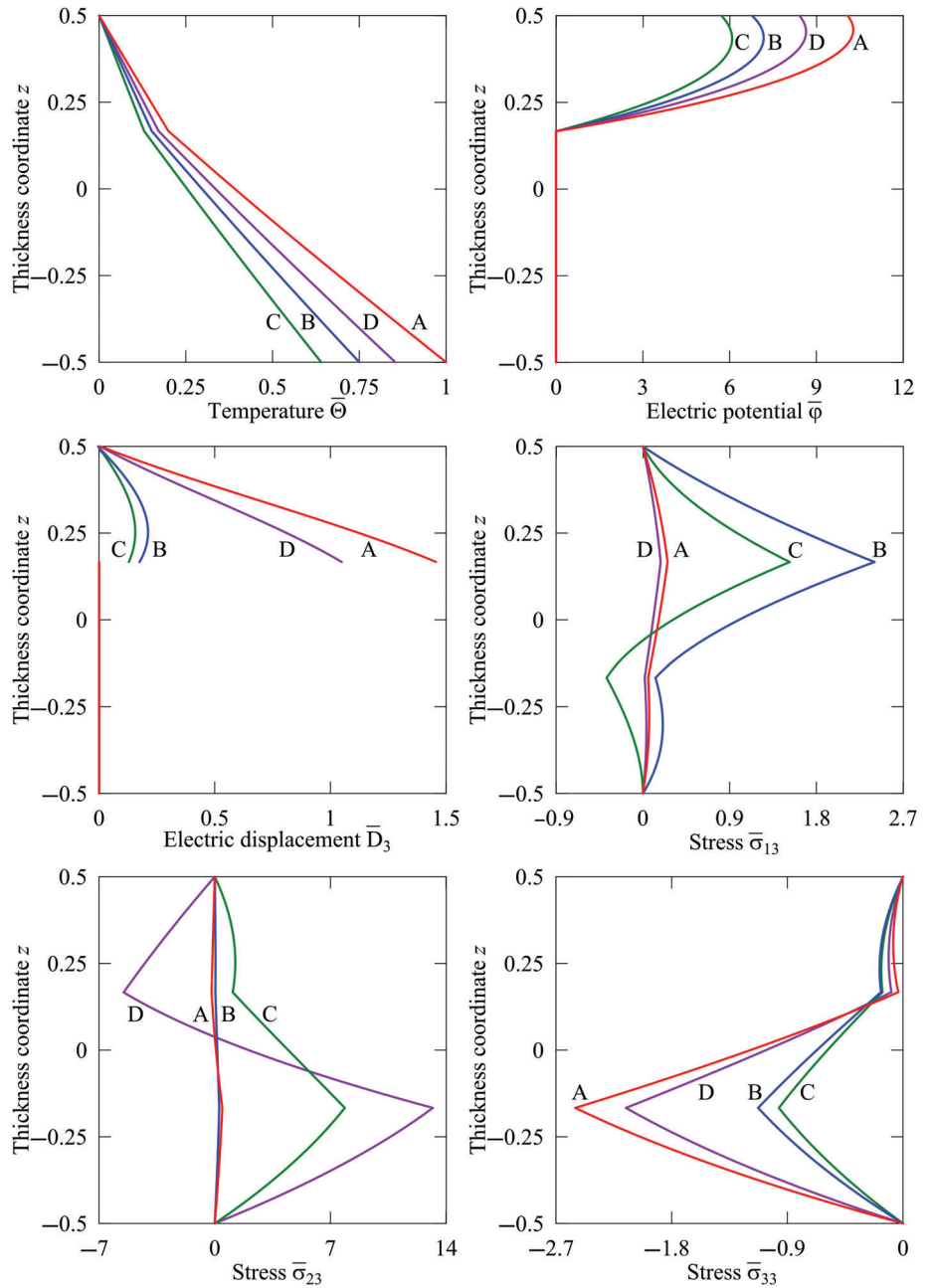
Due to symmetry, only one sixteenth of the shell ( $0 \leq \theta_1 \leq L/2$ ,  $0 \leq \theta_2 \leq \pi/4$ ) is modeled by regular meshes. To analyze the results, we employ dimensionless variables from the previous section and introduce additional variables

$$\bar{\sigma}_{11} = 10\sigma_{11}(P, z)/E_r\alpha_r\Theta_0, \quad \bar{\sigma}_{22} = 10\sigma_{22}(P, z)/E_r\alpha_r\Theta_0$$

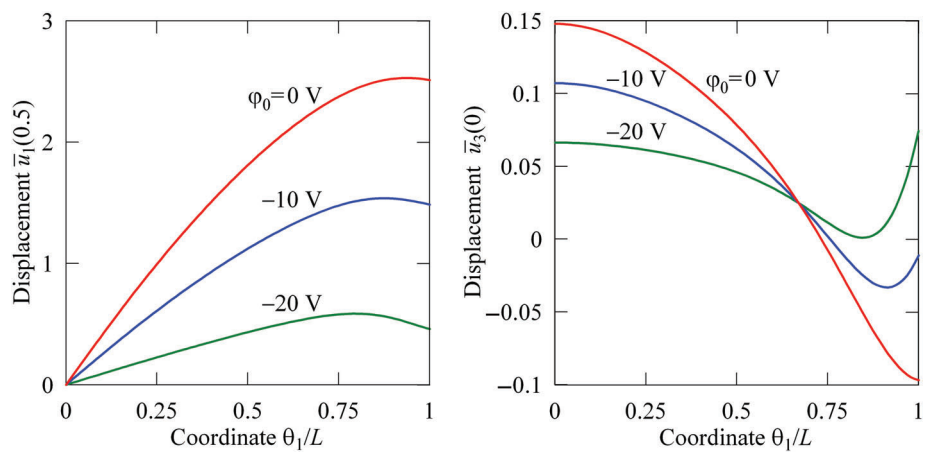
at point P( $L/2, 0$ ) belonging to the middle surface.

Figure 18 shows the dependence of the meridional and transverse displacements of the upper and middle surfaces on the meridional coordinate using five SaS for each layer and  $64 \times 1$  mesh. Figure 19 displays the electric potential, electric displacement and stresses using five SaS for each layer and  $96 \times 1$  mesh. It is seen that the GeXSa4 element correctly describes the boundary conditions on the outer surfaces and the continuity conditions at the interfaces for the transverse stresses in the case of combined loading.

**FIGURE 17** Through-thickness distributions of temperature, electric potential, electric displacement and transverse stresses for a three-layer hyperbolic shell at points A(0,  $\pi/2$ ), B(L/2,  $\pi/2$ ), C(L/2,  $3\pi/8$ ), and D(0,  $3\pi/8$ ) using five SaS for each layer and  $64 \times 64$  mesh



**FIGURE 18** Meridional and transverse displacements of the upper and middle surfaces versus the meridional coordinate for a three-layer hyperbolic shell under combined thermal and electric loading using five SaS for each layer and  $64 \times 1$  mesh



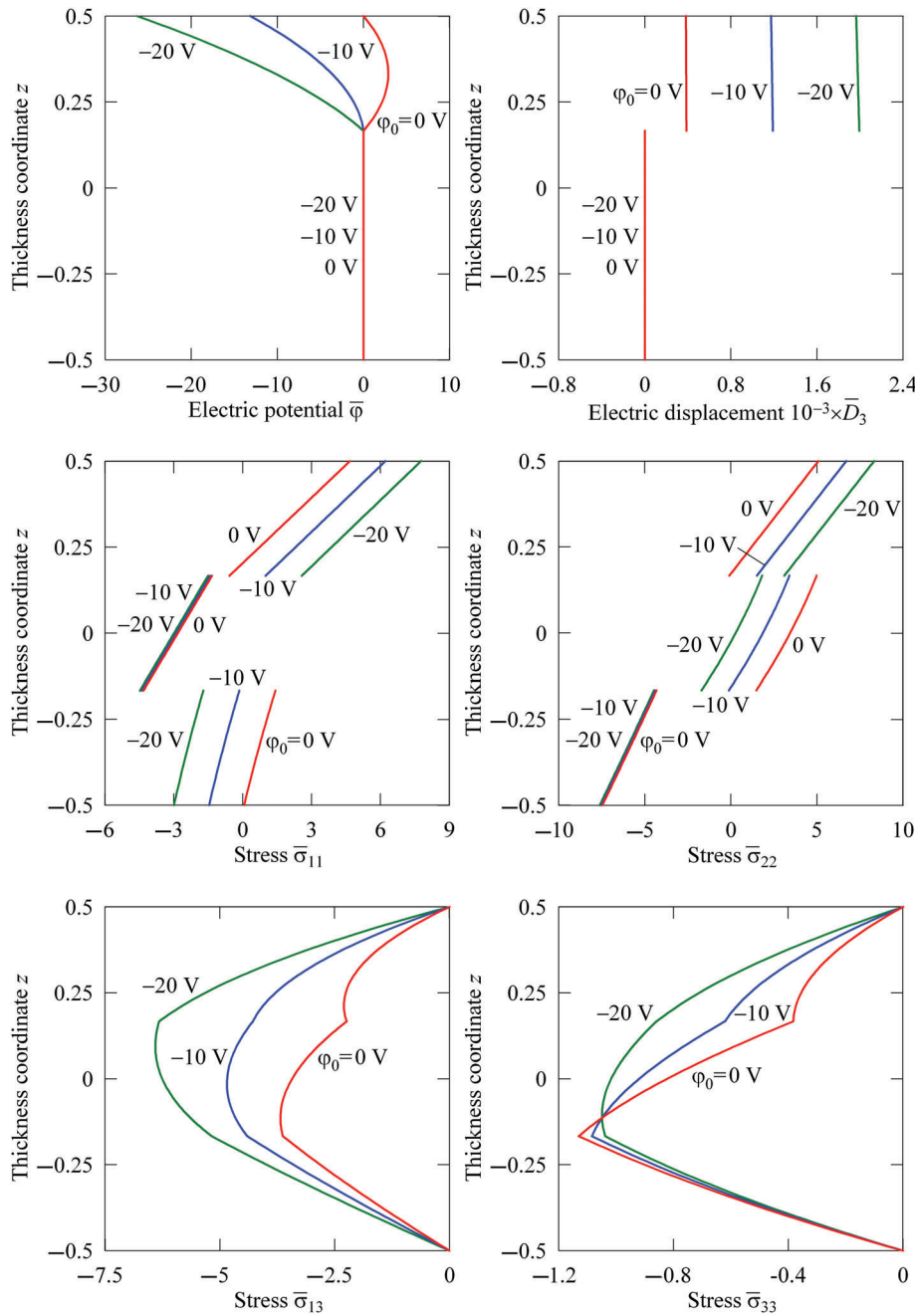


**FIGURE 19** Through-thickness distributions of electric potential, electric displacement and stresses at point  $P(L/2, 0)$  for a three-layer hyperbolic shell under combined thermal and electric loading using five SaS for each layer and  $96 \times 1$  mesh

## 7 | CONCLUSIONS

This paper presents a GeX hybrid-mixed four-node thermopiezoelectric solid-shell element based on the SaS formulation in which temperatures, displacements and electric potentials of SaS are utilized as shell unknowns. The SaS are located at the Chebyshev polynomial nodes within the layers and interfaces as well that significantly improves the behavior of higher-order Lagrange interpolations. To implement efficient analytical integration throughout the element, the extended ANS method for all components of the temperature gradient, strain tensor and electric field vector is applied. The developed thermopiezoelectric solid-shell element exhibits superior performance for coarse meshes due to the exact description of its middle surface. The feature of the proposed GeX hybrid-mixed solid-shell element is that the elemental matrices are evaluated without costly numerical matrix inversion. It can be useful for the 3D analysis of very thick and thin laminated piezoelectric shells under thermo-electro-mechanical loading, since the SaS shell formulation makes it possible to obtain the numerical solutions, which asymptotically approach the solutions of thermopiezoelectricity as a number of SaS tends to infinity.

## ACKNOWLEDGEMENTS

This work was supported by the Russian Science Foundation under Grant No. 18-19-00092.


## CONFLICT OF INTEREST

The authors declare no potential conflict of interest.

## DATA AVAILABILITY STATEMENT

Research data are not shared.

## ORCID

Gennady M. Kulikov  <https://orcid.org/0000-0002-8243-3461>

## REFERENCES

1. Tauchert TR, Ashida F, Noda N, Adali S, Verijenko V. Developments in thermopiezoelasticity with relevance to smart composite structures. *Compos Struct.* 2000;48:31-38.
2. Wu CP, Chiu KH, Wang YM. A review on the three-dimensional analytical approaches of multilayered and functionally graded piezoelectric plates and shells. *Comput Mater Continua.* 2008;8:93-132.
3. Dube GP, Kapuria S, Dumir PC. Exact piezothermoelastic solution of simply-supported orthotropic flat panel in cylindrical bending. *Int J Mech Sci.* 1996;38:1161-1177.
4. Shang F, Wang Z, Li Z. Analysis of thermally induced cylindrical flexure of laminated plates with piezoelectric layers. *Compos Part B.* 1997;28:185-193.
5. Ootao Y, Tanigawa Y. Three-dimensional transient piezothermoelasticity for a rectangular composite plate composed of cross-ply and piezoelectric laminae. *Int J Eng Sci.* 2000;38:47-71.
6. Zhang C, Di S, Zhang N. A new procedure for static analysis of thermo-electric laminated composite plates under cylindrical bending. *Compos Struct.* 2002;56:131-140.
7. Zhang C, Cheung YK, Di S, Zhang N. The exact solution of coupled thermoelectroelastic behavior of piezoelectric laminates. *Comput Struct.* 2002;80:1201-1212.
8. Xu K, Noor AK, Tang YY. Three-dimensional solutions for coupled thermoelectroelastic response of multilayered plates. *Comput Methods Appl Mech Eng.* 1995;126:355-371.
9. Tarn JQ. A state space formalism for piezothermoelasticity. *Int J Solids Struct.* 2002;39:5173-5184.
10. Vel SS, Batra RC. Generalized plane strain thermopiezoelectric analysis of multilayered plates. *J Therm Stress.* 2003;26:353-377.
11. Zhong Z, Shang ET. Exact analysis of simply supported functionally graded piezothermoelectric plates. *J Intel Mater Syst Struct.* 2005;16:643-651.
12. Tarn JQ, Chang HH. A refined state space formalism for piezothermoelasticity. *Int J Solids Struct.* 2008;45:3021-3032.
13. Cheng ZQ, Batra RC. Three-dimensional asymptotic scheme for piezothermoelastic laminates. *J Therm Stress.* 2000;23:95-110.
14. Kulikov GM, Plotnikova SV. Exact 3D thermoelectroelastic analysis of piezoelectric plates through a sampling surfaces method. *Mech Adv Mater Struct.* 2015;22:33-43.
15. Kulikov GM, Plotnikova SV. An analytical approach to three-dimensional coupled thermoelectroelastic analysis of functionally graded piezoelectric plates. *J Intell Mater Syst Struct.* 2017;28:435-450.
16. Xu K, Noor AK. Three-dimensional analytical solutions for coupled thermo-electroelastic response of multilayered cylindrical shells. *AIAA J.* 1996;34:802-810.
17. Kapuria S, Dumir PC, Sengupta S. An exact axisymmetric solution for a simply supported piezoelectric cylindrical shell. *Arch Appl Mech.* 1997;67:260-273.
18. Kapuria S, Sengupta S, Dumir PC. Three-dimensional solution for a hybrid cylindrical shell under axisymmetric thermoelectric load. *Arch Appl Mech.* 1997;67:320-330.
19. Kapuria S, Dumir PC, Sengupta S. Nonaxisymmetric exact piezothermoelastic solution for laminated cylindrical shell. *AIAA J.* 1997;35:1792-1795.
20. Ootao Y, Tanigawa Y. Transient piezothermoelasticity for a cylindrical composite panel composed of cross-ply and piezoelectric laminae. *Int J Mech Sci.* 2002;44:1861-1877.
21. Ootao Y, Tanigawa Y. Transient piezothermoelasticity for a cylindrical composite panel composed of angle-ply and piezoelectric laminae. *Int J Solids Struct.* 2002;39:5737-5752.
22. Kulikov GM, Mamontov AA, Plotnikova SV. Coupled thermoelectroelastic stress analysis of piezoelectric shells. *Compos Struct.* 2015;124:65-76.
23. Kulikov GM, Plotnikova SV. Assessment of the sampling surfaces formulation for thermoelectroelastic analysis of layered and functionally graded piezoelectric shells. *Mech Adv Mater Struct.* 2017;24:392-409.
24. Allik H, Hughes TJR. Finite element method for piezoelectric vibration. *Int J Numer Meth Eng.* 1970;2:151-157.
25. Rao SS, Sunar M. Piezoelectricity and its use in disturbance sensing and control of flexible structures: a survey. *Appl Mech Rev.* 1994;47:113-123.

26. Benjeddou A. Advances in piezoelectric finite element modeling of adaptive structural elements: a survey. *Comput Struct*. 2000;76:347-363.
27. Correia VMF, Gomes MAA, Suleman A, Mota Soares CM, Mota Soares CA. Modelling and design of adaptive composite structures. *Comput Methods Appl Mech Eng*. 2000;185:325-4346.
28. Sanbi M, Saadani R, Sbai K, Rahmoune M. Thermal effects on vibration and control of piezocomposite Kirchhoff plate modeled by finite elements method. *Smart Mater Res*. 2015;748459:1-15.
29. Nanthakumar SS, Lahmer T, Zhuang X, Park HS, Rabczuk T. Topology optimization of piezoelectric nanostructures. *J Mech Phys Solids*. 2016;94:316-335.
30. Lee HJ, Saravanos DA. A mixed multi-field finite element formulation for thermopiezoelectric composite shells. *Int J Solids Struct*. 2000;37:4949-4967.
31. Varelis D, Saravanos DA. Non-linear coupled multi-field mechanics and finite element for active multi-stable thermal piezoelectric shells. *Int J Numer Methods Eng*. 2008;76:84-107.
32. Ganesan N, Kadoli R. Buckling and dynamic analysis of piezothermoelastic composite cylindrical shell. *Compos Struct*. 2003;59:45-60.
33. Rao MN, Schmidt R, Schröder KU. Static and dynamic FE analysis of piezolaminated composite shells considering electric field nonlinearity under thermo-electro-mechanical loads. *Acta Mech*. 2018;229:5093-5120.
34. Gu H, Chattopadhyay A, Li J, Zhou X. A higher order temperature theory for coupled thermo-piezoelectric-mechanical modeling of smart composites. *Int J Solids Struct*. 2000;37:6479-6497.
35. Zhou X, Chattopadhyay A, Gu H. Dynamic responses of smart composites using a coupled thermo-piezoelectric-mechanical model. *AIAA J*. 2000;38:1939-1948.
36. Jiang JP, Li DX. Finite element formulations for thermopiezoelectric laminated composite plates. *Smart Mater Struct*. 2008;17:015027.
37. Kapuria S, Alam N. Coupled efficient zigzag finite element analysis of piezoelectric hybrid beams under thermal loads. *J Therm Stress*. 2006;29:553-583.
38. Phung-Van P, Tran LV, Ferreira AJM, Nguyen-Xuan H, Abdel-Wahab M. Nonlinear transient isogeometric analysis of smart piezoelectric functionally graded material plates based on generalized shear deformation theory under thermo-electro-mechanical loads. *Nonlinear Dyn*. 2017;87:879-894.
39. Lee HJ, Saravanos DA. Coupled layerwise analysis of thermopiezoelectric composite beams. *AIAA J*. 1996;34:1231-1237.
40. Lee HJ. *Finite Element Analysis of Active and Sensory Thermopiezoelectric Composite Materials*. NASA/TM-2001-210892. Cleveland, OH: NASA Glenn Research Center; 2001.
41. Oh IK, Han JH, Lee I. Thermopiezoelectric snapping of piezolaminated plates using layerwise nonlinear finite elements. *AIAA J*. 2001;39:1188-1197.
42. Zappino E, Carrera E. Refined one-dimensional models for the multi-field analysis of layered smart structures. *Adv Struct Mater*. 2018;81:343-366.
43. Zappino E, Carrera E. Thermo-piezo-elastic analysis of amplified piezoceramic actuators using a refined one-dimensional model. *J Intell Mater Syst Struct*. 2018;29:3482-3494.
44. Tan XG, Vu-Quoc L. Optimal solid shell element for large deformable composite structures with piezoelectric layers and active vibration control. *Int J Numer Methods Eng*. 2005;64:1981-2013.
45. Klinkel S, Wagner W. A geometrically non-linear piezoelectric solid shell element based on a mixed multi-field variational formulation. *Int J Numer Methods Eng*. 2006;65:349-382.
46. Schulz K, Klinkel S, Wagner W. A finite element formulation for piezoelectric shell structures considering geometrical and material non-linearities. *Int J Numer Methods Eng*. 2011;87:491-520.
47. Lentzen S. *Nonlinearly Coupled Thermopiezoelectric Modelling and FE-Simulation of Smart Structures*. Fortschritt-Berichte VDI, Reihe 20, Nr. 419. Düsseldorf, Germany: VDI Verlag; 2009.
48. Schmidt R, Rao MN, Schröder KU. Geometrically nonlinear and coupled thermopiezomechanical modeling and analysis of smart FGM plates and shells. In: Zingoni A, ed. *Insights and Innovations in Structural Engineering, Mechanics and Computation*. London, UK: Taylor & Francis; 2016:407-413.
49. Kulikov GM, Plotnikova SV. Solution of a coupled problem of thermo-piezoelectricity based on a geometrically exact shell element. *Mech Compos Mater*. 2010;46:349-364.
50. Kulikov GM, Plotnikova SV. Finite rotation piezoelectric exact geometry solid-shell element with nine degrees of freedom per node. *Comp Mater Continua*. 2011;23:233-264.
51. Kulikov GM, Plotnikova SV. The use of 9-parameter shell theory for development of exact geometry 12-node quadrilateral piezoelectric laminated solid-shell elements. *Mech Adv Mater Struct*. 2015;22:490-502.
52. Kulikov GM, Plotnikova SV. Finite rotation exact geometry solid-shell element for laminated composite structures through extended SaS formulation and 3D analytical integration. *Int J Numer Methods Eng*. 2019;119:852-878.
53. Rao SS, Sunar M. Analysis of distributed thermopiezoelectric sensors and actuators in advanced intelligent structures. *AIAA J*. 1993;31:1280-1286.
54. Tzou HS, Ye R. Piezothermoelasticity and precision control of piezoelectric systems: theory and finite element analysis. *J Vibr Acoust*. 1994;116:489-495.
55. Görnandt A, Gabbert U. Finite element analysis of thermopiezoelectric smart structures. *Acta Mech*. 2002;154:129-140.
56. Shang F, Kuna M, Scherzer M. A finite element procedure for three-dimensional analysis of thermopiezoelectric structures in static applications. *Tech Mech*. 2002;22:235-243.

57. Song G, Zhou X, Binienda W. Thermal deformation compensation of a composite beam using piezoelectric actuators. *Smart Mater Struct.* 2004;13:30-37.
58. Tian X, Zhang J, Shen Y, Lu TJ. Finite element method for generalized piezothermoelastic problems. *Int J Solids Struct.* 2007;44:6330-6339.
59. Kulikov GM, Plotnikova SV. Exact geometry SaS solid-shell element for 3D stress analysis of FGM piezoelectric structures. *Curved Layered Struct.* 2018;5:116-135.
60. Kulikov GM, Plotnikova SV, Glebov AO. Assessment of nonlinear exact geometry SaS solid-shell elements and ANSYS solid elements for 3D stress analysis of piezoelectric shell structures. *Int J Numer Methods Eng.* 2020;121:3795-3823.
61. Kulikov GM, Plotnikova SV, Carrera E. Modeling and analysis of spiral actuators by exact geometry piezoelectric solid-shell elements. *J Intel Mater Syst Struct.* 2020;31:53-70.
62. Pian THH, Sumihara K. Rational approach for assumed stress finite elements. *Int J Numer Methods Eng.* 1984;20:1685-1695.
63. Hoa SV, Feng W. *Hybrid Finite Element Method for Stress Analysis of Laminated Composites.* New York, NY: Springer Science; 1998.
64. Kulikov GM, Plotnikova SV. Heat conduction analysis of laminated shells by a sampling surfaces method. *Mech Res Commun.* 2014;55:59-65.
65. Reddy JN. *Mechanics of Laminated Composite Plates and Shells: Theory and Analysis.* 2nd ed. Boca Raton, FL: CRC Press; 2004.

**How to cite this article:** Kulikov GM, Plotnikova SV. Coupled thermoelectroelastic analysis of thick and thin laminated piezoelectric structures by exact geometry solid-shell elements based on the sampling surfaces method. *Int J Numer Methods Eng.* 2021;122:2446–2477. <https://doi.org/10.1002/nme.6627>

## APPENDIX A

Here, we present some elemental matrices used in Section 3. The nodal thermal matrices  $\mathbf{B}_{\theta r}^{(n)i_n}$  introduced in Equation (19) to determine the temperature gradients on SaS of the  $n$ th layer at element nodes can be written using Equations (8), (16), (19), and (20) as

$$\begin{aligned} \left( \mathbf{B}_{\theta r}^{(n)i_n} \right)_{\alpha, 1+\mu_n+N_{\text{SaS}}(s-1)} &= \frac{1}{2a_\alpha A_{\alpha r} c_{\alpha r}^{(n)i_n}} n_{\alpha s}, \\ \left( \mathbf{B}_{\theta r}^{(n)i_n} \right)_{3, 1+\nu_n+N_{\text{SaS}}(s-1)} &= \delta_{rs} M^{(n)j_n} \left( \theta_3^{(n)i_n} \right), \\ \mu_n &= i_n + \sum_{\gamma=1}^{n-1} I_\gamma - n, \quad \nu_n = j_n + \sum_{\gamma=1}^{n-1} I_\gamma - n, \end{aligned} \quad (\text{A1})$$

where  $A_{\alpha r}$ ,  $k_{\alpha r}$  and  $c_{\alpha r}^{(n)i_n} = 1 + k_{\alpha r} \theta_3^{(n)i_n}$  are the nodal values of geometric parameters of the shell element;  $2a_1$  and  $2a_2$  are the lengths of the element (Figure 2);  $\delta_{rs}$  is the Kronecker delta. The coefficients  $n_{\alpha s}$  are defined by Equation (17) and, as we remember, the indices  $n = 1, 2, \dots, N$ ;  $i_n, j_n = 1, 2, \dots, I_n$ ;  $r, s = 1, 2, 3, 4$  and  $\alpha = 1, 2$ . The remaining components of matrices  $\mathbf{B}_{\theta r}^{(n)i_n}$  not written out explicitly are zero.

The stiffness matrix  $\mathbf{K}_{\theta\theta}^c$  corresponding to the convective heat transfer from Equation (24) is given by

$$\begin{aligned} \left( \mathbf{K}_{\theta\theta}^c \right)_{1+N_{\text{SaS}}(r-1), 1+N_{\text{SaS}}(s-1)} &= \bar{c}_1^- \bar{c}_2^- h^- R_{rs}, \\ \left( \mathbf{K}_{\theta\theta}^c \right)_{rN_{\text{SaS}}, sN_{\text{SaS}}} &= \bar{c}_1^+ \bar{c}_2^+ h^+ R_{rs}, \end{aligned} \quad (\text{A2})$$

$$R_{rs} = \frac{1}{4} \int_{-1}^1 \int_{-1}^1 N_r N_s d\xi_1 d\xi_2, \quad (\text{A3})$$

where  $\bar{c}_\alpha^- = 1 - \bar{k}_\alpha h/2$  and  $\bar{c}_\alpha^+ = 1 + \bar{k}_\alpha h/2$  are the components of the shifter tensor on the bottom and top surfaces at the element center.

The element-wise thermal surface vector  $\mathbf{F}_\theta$  from Equation (24) is written as

$$\mathbf{F}_\theta = [\mathbf{F}_{\theta 1}^T \ \mathbf{F}_{\theta 2}^T \ \mathbf{F}_{\theta 3}^T \ \mathbf{F}_{\theta 4}^T]^T, \quad \mathbf{F}_{\theta r} = [f_{\theta r}^- \ 0 \ 0 \ \dots \ 0 \ f_{\theta r}^+]^T, \quad (\text{A4})$$

where

$$f_{\theta r}^- = \frac{1}{4} \overline{\overline{c_1 c_2}} \int_{-1}^1 \int_{-1}^1 N_r \widehat{q}_3^- d\xi_1 d\xi_2, \quad f_{\theta r}^+ = -\frac{1}{4} \overline{\overline{c_1^+ c_2^+}} \int_{-1}^1 \int_{-1}^1 N_r \widehat{q}_3^+ d\xi_1 d\xi_2 \quad (\text{A5})$$

for the prescribed heat flux on the outer surfaces and

$$f_{\theta r}^- = \frac{1}{4} \overline{\overline{c_1 c_2}} h^- \int_{-1}^1 \int_{-1}^1 N_r \widehat{T}_c^- d\xi_1 d\xi_2, \quad f_{\theta r}^+ = \frac{1}{4} \overline{\overline{c_1^+ c_2^+}} h^+ \int_{-1}^1 \int_{-1}^1 N_r \widehat{T}_c^+ d\xi_1 d\xi_2 \quad (\text{A6})$$

in the case of the convective heat transfer.

## APPENDIX B

The nodal piezoelectric matrices  $\mathbf{B}_{\varphi r}^{(n)i_n}$  introduced in Section 5 to define the electric field of SaS of the  $n$ th layer at element nodes (47) can be written in a closed form. Using Equations (30), (42), (47), and (48) leads to

$$\begin{aligned} \left( \mathbf{B}_{\varphi r}^{(n)i_n} \right)_{\alpha, 1+\mu_n+N_{\text{SaS}}(s-1)} &= \frac{1}{2\alpha A_{ar} c_{ar}^{(n)i_n}} n_{as}, \\ \left( \mathbf{B}_{\varphi r}^{(n)i_n} \right)_{3, 1+\nu_n+N_{\text{SaS}}(s-1)} &= \delta_{rs} M^{(n)j_n} \left( \theta_3^{(n)i_n} \right), \\ \mu_n &= i_n + \sum_{\gamma=1}^{n-1} I_\gamma - n, \quad \nu_n = j_n + \sum_{\gamma=1}^{n-1} I_\gamma - n, \end{aligned} \quad (\text{B1})$$

where  $A_{ar}$ ,  $k_{ar}$ , and  $c_{ar}^{(n)i_n}$  are the nodal values of geometric parameters of the shell element utilized in Appendix A. The components of matrices  $\mathbf{B}_{\varphi r}^{(n)i_n}$  not written out explicitly are zero.

The mechanical and electric surface vectors  $\mathbf{F}_u$  and  $\mathbf{F}_\varphi$  from Equations (60) and (61) are defined as

$$\mathbf{F}_u = [\mathbf{F}_{u1}^T \mathbf{F}_{u2}^T \mathbf{F}_{u3}^T \mathbf{F}_{u4}^T]^T, \quad \mathbf{F}_{ur} = [f_{1r}^- f_{2r}^- f_{3r}^- 00 \dots 0 f_{1r}^+ f_{2r}^+ f_{3r}^+]^T, \quad (\text{B2})$$

$$\mathbf{F}_\varphi = [\mathbf{F}_{\varphi 1}^T \mathbf{F}_{\varphi 2}^T \mathbf{F}_{\varphi 3}^T \mathbf{F}_{\varphi 4}^T]^T, \quad \mathbf{F}_{\varphi r} = [f_{\varphi r}^- 00\dots 0 f_{\varphi r}^+]^T, \quad (\text{B3})$$

where

$$f_{ir}^- = -\frac{1}{4} \overline{\overline{c_1 c_2}} \int_{-1}^1 \int_{-1}^1 N_r \widehat{\sigma}_{i3}^- d\xi_1 d\xi_2, \quad f_{ir}^+ = \frac{1}{4} \overline{\overline{c_1^+ c_2^+}} \int_{-1}^1 \int_{-1}^1 N_r \widehat{\sigma}_{i3}^+ d\xi_1 d\xi_2, \quad (\text{B4})$$

$$f_{\varphi r}^- = -\frac{1}{4} \overline{\overline{c_1 c_2}} \int_{-1}^1 \int_{-1}^1 N_r \widehat{D}_3^- d\xi_1 d\xi_2, \quad f_{\varphi r}^+ = \frac{1}{4} \overline{\overline{c_1^+ c_2^+}} \int_{-1}^1 \int_{-1}^1 N_r \widehat{D}_3^+ d\xi_1 d\xi_2. \quad (\text{B5})$$

## APPENDIX C

The differential equation of the axisymmetric heat conduction problem for a single-layer sphere can be expressed as

$$\frac{d^2 \Theta}{d\zeta^2} + \frac{2}{\zeta} \frac{d\Theta}{d\zeta} = 0, \quad (\text{C1})$$

where  $\zeta \in [R_1, R_2]$  is the radial coordinate;  $R_1 = R - h/2$  and  $R_2 = R + h/2$  are the inner and outer radii of the sphere. The solution of Equation (C1) is written as

$$\Theta = A + \frac{B}{\zeta}. \quad (\text{C2})$$

Substituting Equation (C2) in boundary conditions (77), we obtain

$$A = \frac{\alpha^+ R_2^2 (1 + \alpha^- R_1)}{d} \Theta_0, \quad B = -\frac{\alpha^- \alpha^+ R_1^2 R_2^2}{d} \Theta_0, \quad (C3)$$
$$d = \alpha^- R_1^2 + \alpha^+ R_2^2 + \alpha^- \alpha^+ h R_1 R_2.$$

Due to Equations (5) and (C2), the heat flux is

$$q_3 = k_{33} \frac{B}{\zeta^2}. \quad (C4)$$

Using the radial temperature distribution (C2) and (C3) in the governing equations of the theory of thermopiezoelectricity, we can obtain an analytical solution of the axisymmetric problem for the piezoelectric sphere. This can be done using the Symbolic Math Toolbox, which incorporates symbolic computations into the numeric environment of MATLAB.